I give permission for public access to my thesis and for any copying to be done at the discretion of the archives librarian and/or the College librarian.

_____ _____

Signature Date

A STUDY OF IRON OXIDE AND TOPO-CAPPED SILVER NANOPARTICLES

by

Jennifer A. Soltis

A senior thesis submitted to the faculty of

Mount Holyoke College

in partial fulfillment of the requirements for the degree of

Bachelor of Arts

Department of Chemistry

Mount Holyoke College

May 2010

ACKNOWLEDGEMENTS

There are many people who have supported the work that has gone into this thesis. I would like to thank foremost my thesis advisor, Prof. Himali Jayathilake, for her support and guidance of the research presented in the second chapter and throughout the thesis-writing process. I would also like to thank Prof. Megan Núñez and the Núñez Research Group and Prof. Wei Chen and the Chen Research Group for their support and the use of their laboratory resources.

This work was also supported by Thomas Houle and Marian Rice of the Mount Holyoke College Department of Chemistry. FTIR data were gathered with the help of Kristin Shrout and Prof. Dula Amarasiriwardena of Hampshire College (Amherst, MA). This research was supported by a MHC Start-up Grant and the Department of Chemistry.

Direction and support for the research presented in the first chapter were provided by Prof. R. Lee Penn and the Penn Research Group at the University of Minnesota. Prof. Penn also assisted in revising the manuscript. Research performed at the University of Minnesota was supported by the Lando/NSF REU program, the Department of Chemistry, the National Nanotechnology Infrastructure Network (NNIN), and the NSF (Geosciences, CAREER).

Finally, I would like to thank my parents, Thomas and Susan Soltis, and Erin Phillips for their help in editing my final drafts and their constant support along the way.

Table of Contents

List of Figures

List of Tables

I saw that one enquiry only gave occasion to another, that book referred to book, that to search was not always to find, and to find was not always to be informed . . . I set limits to my work, which would in time be ended, though not completed.

Samuel Johnson, Preface to Volume I of his dictionary
Quoted in Winchester, Simon. *The Meaning of Everything: The story of the Oxford English Dictionary*. Oxford University Press: Oxford, 2003. 94-95.

Introduction: An Overview of Nanoparticle Research

Nanoparticles, small crystals or clusters of atoms in the size range of 10^{-9} to 10^{-7} m, have become the focus of many areas in chemistry and materials science research in the last few decades. They are actively used in work involving optics, electronics, catalysis, ceramics, magnetic data storage, nanocomposites, color imaging, bioprocessing, and ferrofluids.[1] Silver nanoparticles are embedded in modern commercial products, such as Sharper Image's FresherLonger™ food storage containers, to take advantage of their antimicrobial properties.[2,3] Gold nanoparticles are being investigated for applications in cancer detection and treatment,[4] while iron oxide nanoparticles can be used for recording magnetic devices.[5] Some nanoparticles fluoresce, for instance, CdSe quantum dots (semiconducting nanoparticles),[1] while others phosphoresce, like a class of recently developed particles formed by encapsulating phosphorescent molecules (e.g., the metal chelates platinum, palladium, and ruthenium) with halogen-

[1] Wang, Z. L, Ed. *Characterization of Nanophase Materials*. Wiley-VCH: New York, 2000.
[2] "Sharper Image Introduces FresherLonger™ Miracle Food Storage Containers." Business Wire. March 8, 2006. Accessed April 20, 2010. <http://www.nsti.org/press/PRshow.html?id=867>
3 Rai, M; Yadav, A; Gade, A. "Silver nanoparticles as a new generation of antimicrobials." *Biotechnol. Adv.* **2009**, 27, 76-83.
[4] Cai, W; Gao, T; Hong, H; Sun, J. "Applications of gold nanoparticles in cancer nanotechnology." *Nanotechnol., Sci. Appl.* **2008,** *1*, 17–32.
[5] Skumryev, V; Stoyanov, S; Zhang, Y; Hadjipanayis, G; Givord, D; Nogués, J. "Beating the superparamagnetic limit with exchange bias." *Nature* **2003**, *423I*, 850-853.

containing polymers.[6] These behaviors, particularly for optical and electronic properties, are extremely size-dependent.[1] For example, the color of CdSe quantum dots is size-dependent and can be controlled during synthesis by controlling particle size, making them tunable over the entire range of visible light (~400-700 nm).[1] Gold nanoparticles, in a size-dependent range of red colors, have been used in coloring stained glass windows, while different sizes of silver nanoparticles exhibit different hues of yellow.[7]

Nanoparticles also have particularly interesting applications in the field of quantum dynamics: the small physical size of a semiconducting nanoparticle (quantum dot) restricts electron movement, creating a confined electron-hole system with quantized energy levels.[1] A small, spherical, metallic nanoparticle undergoes plasmon resonance when exposed to light, causing its unexpected bright color.[7] Who would expect a gold nanoparticle to appear red? The irradiation experienced by the particle causes its electron cloud to oscillate relative to the nuclear framework of the particle in the direction of the applied electric field.[7,8] Metallic nanoparticles exhibit plasmon resonance in the UV/visible spectral range, giving them a wide range of intense colors.[8] Additionally, the surface atoms of a nanoparticle have reduced coordination numbers, increasing their surface energy and, therefore, reactivity.[1]

---

[6] Song, X; Huang, L; Wu, B. "Bright and Monodispersed Phosphorescent Particles and Their Applications for Biological Assays." *Anal. Chem.* **2008**, *80*, 5501-5507.
[7] Kelly, K. L; Coronado, E; Zhao, L. L; Schatz, G. C. "The Optical Properties of Metal Nanoparticles: The Influence of Size, Shape, and Dielectric Environment." *J. Phys. Chem. B* **2003**, *107*, 668-677.
[8] Zhang, Q; Tan, Y. N; Xie, J; Lee, J. Y; "Colloidal Synthesis of Plasmonic Metal Nanoparticles." *Plasmonics* **2009**, *4*, 9-22.

When particles are small enough, on the scale of tens to hundreds of nanometers in length, they begin to behave in entirely different ways from their bulk parent material. Nanoparticles represent the transition between individual atoms and bulk material properties.[1] Nano-scale materials may possess different melting points than their bulk equivalents, as is the case with gold, which melts at 300°C for particles with a diameter of <5 nm, compared to 1063°C for bulk gold.[1] At a gross optical scale, nanoparticles also scatter light in different wavelengths. As previously mentioned, some quantum dots can have their color very precisely controlled by controlling particle size.

Research in nanoparticle behavior and nanotechnology is a vibrant, active field that spans the disciplines of chemistry, physics, biology, and materials science. Scientists are interested in synthesizing nanoparticles and controlling their size and morphology to manipulate their optical, electronic, and magnetic properties. They can then be used in the manufacture of nanocomposite structures and examined for physical and chemical behavior both as individual particles and in multi-particle systems.

Working with samples smaller than the wavelength of visible light presents special imaging challenges—light microscopes do not have sufficient resolution to “see” such small objects.[1] A wide range of instruments has been developed to characterize nanoparticles (and other small things) based on size, topography, electron-scattering affinity, magnetic field, and a host of other physical properties. This work looks at two microscopy techniques in particular, transmission electron microscopy (TEM) and atomic force microscopy (AFM).

Other common methods of nanoparticle characterization include, but are not limited to, scanning electron microscopy (for 3-dimensional imaging),[1] X-ray diffraction and small-angle X-ray scattering (XRD/SAXS, for determining crystalline structure),[1] dynamic light scattering (for measurement of hydrodynamic radius),[9] and scanning tunneling electron microscopy (STEM, for characterization of structural, chemical, and morphological information).[1]

This work examines two different areas in nanoparticle research and the characterization techniques important for those projects. It is divided into two chapters addressing separate projects on nanoparticle and nanocomposite synthesis and characterization. It begins at the level of individual nanoparticles by looking at an iron oxide nanoparticle system and traces the growth and phase transformation of individual nanoparticles as they assemble to form nanorods of a different iron oxide species. The next chapter broadens the scale of focus to a nanocomposite system where capped silver nanoparticles are assembled into larger structures, namely, Langmuir-Schaefer monolayers.

The first chapter examines the synthesis of ferrihydrite nanoparticles, a poorly crystalline iron oxide, and their subsequent kinetics of growth and phase transformation. Treatment of a ferrihydrite suspension with solutions of phosphate, Fe(II), sugar, and alizarin (a catechol) slows or stops the oriented aggregation of ferrihydrite nanoparticles into goethite nanorods, a more stable crystalline, antiferromagnetic iron oxide.[10,11,12] These chemical additives can also affect rod

---

[9] "Zetasizer Nano Series User Manual." MAN0317, Issue 2.1. Malvern Instruments Ltd. Worcestershire, United Kingdom. July 2004.
[10] Cornell, R. M; Schwertmann, U. *The iron oxides: structure, properties, reactions, occurrences and uses*. Wiley VCH: New York, 2003.

morphology (Fe(II) and sugar) or additionally trigger the formation of hematite, another crystalline, antiferromagnetic species[13] (sugar). The instrumental focus of this chapter is the transmission electron microscope (TEM), which was used extensively in the determination of growth kinetics of these nanoparticles.

The second chapter looks at the manufacture of tri-*n*-octylphosphine oxide (TOPO)-capped silver nanoparticles into Langmuir-Schaefer monolayers. Monolayers of 12 nm particles were horizontally deposited onto mica sheets. The layers were deposited over a range of different trough surface pressures to influence packing density. They were then analyzed via atomic force microscopy (AFM), to gain information about particle arrangement and monolayer height, and Fourier transform infrared spectroscopy (FTIR), to confirm the characteristic vibrational modes of TOPO. The instrumental focus for this chapter addresses the theory and use of the Langmuir trough and AFM.

---

[11] Schwertmann, U; Cornell, R. M. *Iron Oxides in the Laboratory: Preparation and Characterization*. VCH Publishers, Inc.: New York, 1991.
[12] Penn, R. L; Erbs, J. J; Gulliver, D. M. Controlled growth of alpha-FeOOH nanorods by exploiting-oriented aggregation. *J. Cryst. Growth* **2006**, *293*, 1-4.
[13] Moskowitz, B. M. "Hitchhiker's Guide to Magnetism." Institute for Rock Magnetism, University of Minnesota, 1991. Accessed March 2010. <http://www.irm.umn.edu/hg2m/hg2m_index.html>

Chapter 1: The Effects of Surface-Active Species on Ferrihydrite Growth and Phase Transformation

Introduction

Iron oxides are naturally occurring iron minerals that can be found throughout the Earth's surface and crust. The sixteen known iron oxides and oxyhydroxides[1] enter the environment through rock weathering, Fe(II) and Fe(III) redox reactions, and precipitation/hydrolysis reactions.[2] They range in color from yellow to red, brown, or black[3] and come in sizes of a few to several hundred nanometers.[2] In addition to being present in soils and rocks, they are also found in rivers, lakes, and the seafloor. They have high redox reactivity and surface adsorptivity, which gives them an important role in the transformation and mobility of arsenic, heavy metals, and anthropogenic contaminants.[2,3] They have also been found admixed to Aeolian Sahara dust and are active in biological organisms.[3]

Ferrihydrite (Fh, $Fe_5HO_8 \cdot 4H_2O$)[1] is a poorly crystalline iron oxide nanoparticle that can be deposited on the earth's surface by ferriferous springs or produced by changing the pH of ferric-rich water or oxidizing ferrous-rich water.[1]

---

[1] Cornell, R. M; Schwertmann, U. *The iron oxides: structure, properties, reactions, occurrences and uses*. Wiley VCH: New York, 2003.
[2] Erbs, J. J; Gilbert, B; Penn, R. L. Influence of Size on Reductive Dissolution of Six-Line Ferrihydrite. *J. Phys. Chem. C* **2008**, *112*, 12127-12133.

This highly reactive iron oxide species is reddish-brown in color and has important uses in industry for the production of clays and ceramic materials. It is also biologically active in the form of ferritin, a protein-ferrihydrite complex necessary for iron storage in living organisms.[3]

There are two types of ferrihydrite species, 2-line and 6-line, whose names refer to the number of peaks observed in their powder X-ray diffraction patterns, indicating that the compounds have different degrees of structural order.[2,3,4] Six-line ferrihydrite particles produced in a laboratory setting range in size from 4 to 9 nm, and particle size is dependent on synthesis temperature.[5] Recent work has determined a hexagonal space group $P6_3mc$ for particles across sample sets with average particle lengths of 2, 3, and 6 nm. Although there are slight changes in lattice parameters and occupancy with size, the underlying structure is not size-dependent.[4]

Ferrihydrite is one of the most reactive iron oxide species[6] and serves as a precursor mineral to the most thermodynamically stable iron oxides, goethite (α-FeOOH) and hematite (Fe_2O_3).[1,2,3] Goethite is a yellow-brown, crystalline, antiferromagnetic iron oxyhydroxide,[1,3,7] while red-colored hematite is a

---

[3] Schwertmann, U; Cornell, R. M. *Iron Oxides in the Laboratory: Preparation and Characterization*. VCH Publishers, Inc.: New York, 1991.
[4] Michel, F. M; Ehm, L; Antao, S. M; Lee, P. L; Chupas, P. J; Liu, G; Strongin, D. R; Schoonen, M. A. A; Phillips, B. L; Parise, J. B. The Structure of Ferrihydrite, a Nanocrystalline Material. *Science* **2007**, *316*, 1726-1729.
[5] Penn, R. L; Tanaka, K; Erbs, J. Size dependent kinetics of oriented aggregation. *J. Cryst. Growth* **2007**, *309*, 97-102.
[6] Kung, K.-H; McBride, M. B. Electron transfer processes between hydroquinone and iron oxides. *Clays Clay Miner.* **1988**, *36*, 303
[7] Penn, R. L; Erbs, J. J; Gulliver, D. M. Controlled growth of alpha-FeOOH nanorods by exploiting-oriented aggregation. *J. Cryst. Growth* **2006**, *293*, 1-4.

crystalline canted antiferromagnet.[8] Goethite can be synthesized by aging suspension of ferrihydrite. Conversion can occur slowly, at room temperature, or be accelerated by aging at moderate temperatures, ~80°C.[9] The size of the resulting nanorods, tens of nanometers in length, depends on the size of the primary ferrihydrite particles. This occurs via phase transformation of the particles from ferrihydrite to goethite, followed by their oriented aggregation into larger crystals. Crystal growth can also occur via coarsening (Ostwald ripening), but oriented aggregation dominates the ferrihydrite-goethite system.[5,10]

Transmission electron microscopy (TEM) supports the oriented aggregation mechanism. If Ostwald ripening were to occur, the presence of dimples and defects along the edges of the crystals would not be expected. However, when seen in transmission electron micrographs, goethite rods have edge defects, which suggests oriented aggregation.[11] The ferrihydrite particles have aligned but the round shapes of the precursor particles have not been fully smoothed into the flat edges of goethite rods.[11]

This model is also supported by recent work indicating a mesocrystal intermediate in this transformation.[10] A mesocrystal intermediate is formed when the primary particles have aligned in a crystallographic manner but have not yet

---

[8] Moskowitz, B. M. "Hitchhiker's Guide to Magnetism." Institute for Rock Magnetism, University of Minnesota, 1991. Accessed March 2010. <http://www.irm.umn.edu/hg2m/hg2m_index.html>
[9] Burleson, D. J; Penn, R. L. Two-Step Growth of Goethite from Ferrihydrite. *Langmuir* **2006**, *22*, 402-409.
[10] Yuwono, V. M; Burrows, N. D; Soltis, J. A; Penn, R. L. Oriented Aggregation: Formation and Transformation of Mesocrystal Intermediates Revealed. *J. Am. Chem. Soc.* **2010**, *132*, 2163–2165.
[11] Penn, R. L. Kinetics of Oriented Aggregation. *J. Phys. Chem. B* **2004**, *108*, 12707-12712.

formed any crystalline linking material between the individual nanocrystals.[10,12] Cryogenic TEM images show primary particles oriented in rod formations with no evidence of crystalline material linking the particles together.[10] Figure 1[10] is a cryogenic TEM image of goethite mesocrystals in which the alignment of individual small particles is readily visible.

The growth of goethite rods occurs via a three-step kinetic model following a second order rate law.[11]

$$P + P \rightarrow P \cdots P \qquad k_1 \qquad (1)$$

$$P \cdots P \rightarrow P + P \qquad k_{-1} \qquad (2)$$

$$P \cdots P \underset{-xH_2O}{\rightarrow} P - P \qquad k_2 \qquad (3)$$

$$d[P-P]/dt = \frac{k_1 k_2}{k_{-1}}[P]^2 \qquad (4)$$

Two primary particles engage in non-bonding particle-particle interactions (eq 1). This association may be reversed, with no net change in secondary crystal production (eq 2), or may proceed to irreversibly form an oriented aggregate (eq 3). When rapid equilibrium is assumed, the reaction follows a second-order rate law with respect to the concentration of primary nanoparticles (eq 4).[11] The growth of the secondary structure also depends on the removal of any solvent molecules adsorbed at the particle interface; otherwise, they will either be incorporated into the bulk particle or prevent oriented aggregation altogether.[5,11]

Because the removal of adsorbed foreign species is necessitated for secondary particle growth by oriented aggregation, the addition of chemical species to an aqueous suspension of ferrihydrite can modify the rate of goethite

[12] Niederberger, M; Cölfen, H. Oriented attachment and mesocrystals: Non-classical crystallization mechanisms based on nanoparticle assembly. *Phys. Chem. Chem. Phys.* **2006**, *8*, 3271-3287.

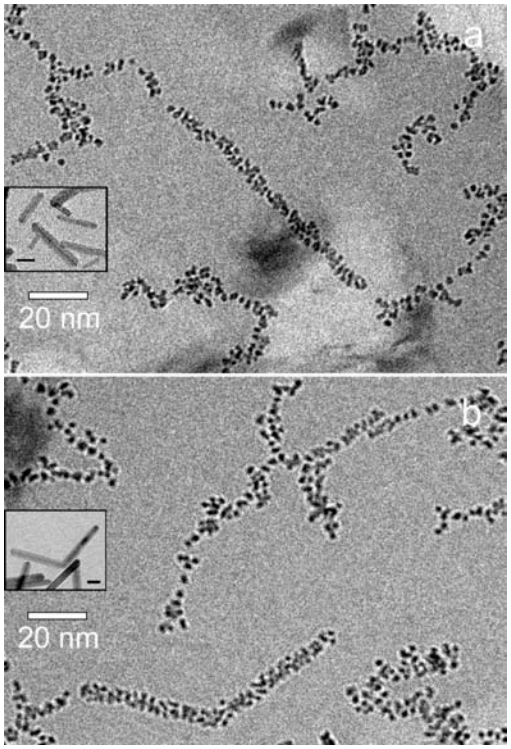

Figure 1: "Cryo-TEM images of mesocrystals with size and shape similar to a product goethite nanorod (a) and twin (b) taken after 15 days of aging. Insets are dry TEM images of product goethite crystals for shape and size comparisons. The scale bars in the insets both correspond to 20 nm."[10]

growth. The goal of this work was to determine how the ferrihydrite-to-goethite growth rate and phase transformation change as the particles are aged in aqueous suspensions treated with surface-active chemical species. This project compares aqueous suspensions of ferrihydrite treated with sugar, Fe(II), phosphate, and alizarin (a catechol) with an untreated sample, all aged at 80°C. Samples were not controlled for oxidation and were all stored in air. Crystallinity of the aged samples was determined via X-ray diffraction (XRD). Growth rates were quantified via measurements of calibrated transmission electron micrographs.

Experimental

Transmission Electron Microscopy

Transmission electron microscopy (TEM) uses an electron beam to produce magnified images of biological and material samples. The development of the electron microscope (both scanning and transmission) presented significant improvement over the magnification limits set by a light microscope. Even with a modern light microscope, maximum resolution is limited by the wavelength of visible light. With a good light microscope and a monochromatic light source, images with a resolving power of half a wavelength can be produced—a maximum resolving power of 200 nm for a visible light microscope.[13,14] This resolution limit is insufficient for discerning nanometer-scale detail. An object must interact with a light beam through reflection or refraction—any object that does not scatter light is effectively invisible in a light microscope.[15] Because they are smaller than the wavelength of visible light, nano-scale objects can be "overlooked" by a light microscope. The solution is to use electrons instead of light; the wavelength of the electrons in a modern TEM range from 1 to 4 picometers. This permits the magnification of particles to the atomic level.[13] A scanning electron microscope has a resolving power of 3 nm,[14,16] while the

---

[13] Penn, R. L. "Transmission Electron Microscopy." Accessed December 2008. <http://www.chem.umn.edu/groups/penn/tem.html>

[14] Flegler, S. L; Heckman, J. W. Jr; Klomparens, K. L. *Scanning and Transmission Electron Microscopy: An Introduction*. Oxford University Press: New York. 1993.

[15] Williams, D. B; Carter, C. B. *Transmission Electron Microscopy: A textbook for materials science*. Plenum Press: New York, 1996.

[16] FEI Company. "Magellan XHR Scanning Electron Microscope." <http://www.fei.com/products/scanning-electron-microscopes/magellan.aspx> Accessed February 2010.

highest resolution TEM can reach 0.8Å (0.08 nm).[17] Today, high resolution TEM (HRTEM) is capable of imaging individual columns of atoms within crystals.[15] Figure 2 shows a high-resolution micrograph of a gold nanoparticle in which the direct atomic structure is visible.[18]

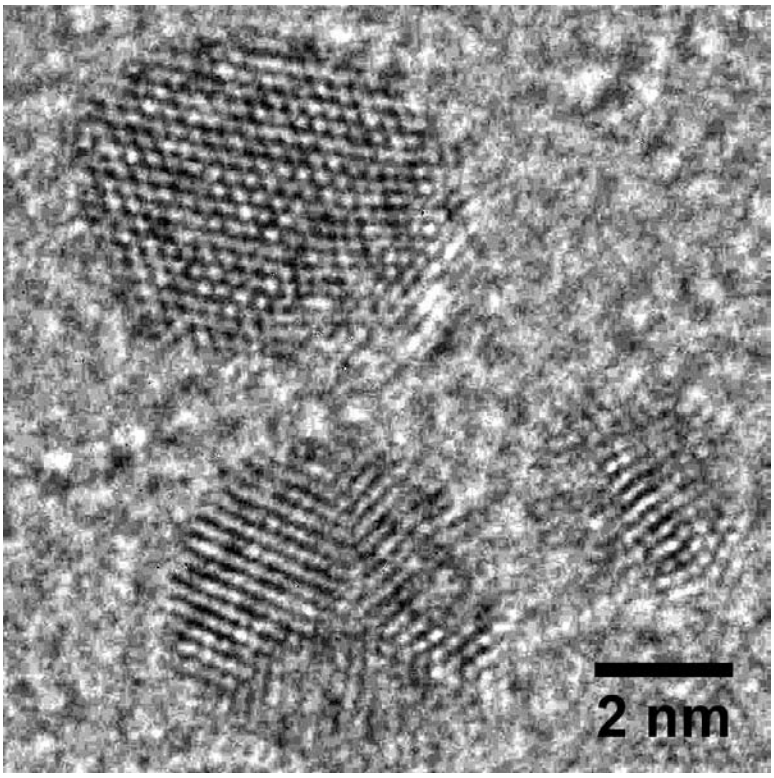

Figure 2: High-resolution TEM of gold nanoparticles. Each small dot within the particle indicates a column of atoms, two atoms wide. These lines are called lattice fringes and indicate crystal structure.

[17] National Center for Electron Microscopy. "Microscopes and Facilities: OÅM." <http://ncem.lbl.gov/frames/oam.htm> Accessed April 2010.
[18] Yuwono, V. M; Burrows, N. D; Soltis, J. A; Penn, R. L. Oriented Aggregation: Formation and Transformation of Mesocrystal Intermediates Revealed. *J. Am. Chem. Soc.* **2010**, *132*, 2163–2165.

The major components of a TEM are the electron source, the lenses, and the image display or image capture device. A schematic of these parts is presented in Figure 3.[19] There are two types of electron sources for TEMs: thermionic and field-emission.[15] One standard thermionic source is the tungsten-hairpin gun. A sufficient voltage is applied across the tungsten filament to produce a cloud of electrons via thermionic emission; the energy applied to the source must be great enough to overcome **Φ** (the work function) of the electrons so they may escape to form an electron beam.[14,15] The choice of tungsten is significant because most materials will melt or vaporize when exposed to so much thermal energy. Tungsten has a high melting temperature (3660 K), which makes it a good choice for this application. Lanthanum hexaboride (LaB_6), which has a low work function, is also suitable (in this case, the crystalline electron source might be called a "cathode," but would not be referred to as a filament).[15] The cathode has a greater negative potential compared to the potential of the gun's aperture, so the electron beam is attracted to the aperture, where some electrons are blocked or deflected and the remainder continue through the microscope's column. The difference in potential between the filament and the aperture is referred to as the scope's accelerating voltage. This voltage determines the energy and wavelength of the electron beam, with a higher voltage providing the shortest wavelength.[15]

In field-emission sources, a high (1-kV) potential is applied to a needle-shaped source. For a tungsten wire with a tip radius of <0.1 μm, a 1-kV potential

[19] "A Review of the Universe" <http://universe-review.ca/I11-41-tem.jpg> Accessed December 2008.

produces an electric field of 10^6 V/m, based on the relationship $E = \frac{V}{r}$, where E is the strength of an electric field produced by a voltage V applied to a spherical point of radius r. This equation models a voltage applied to a spherical point, hence the requirement for a fine, needle-shaped source. The production of this

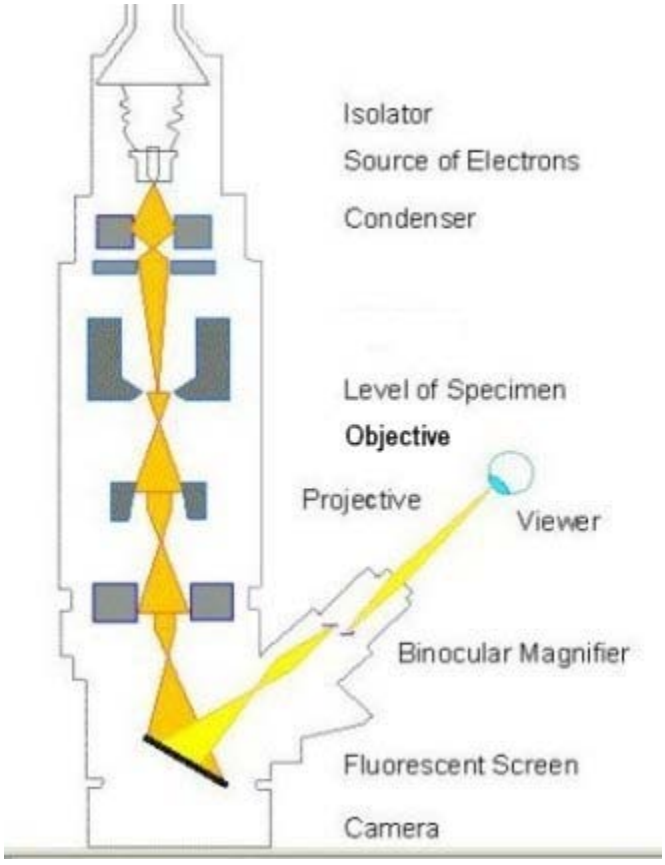

Figure 3: Basic diagram of the structure of a TEM.[19]

electric field lowers the work function barrier and permits electron tunneling from the source. The tip surface must be protected from contaminants either by operating at ambient temperature under ultra-high vacuum or by operating at ambient pressure under elevated temperature.[15]

After the electron beam has been produced, it must be focused to a diameter of <10 nm.[15] Magnification through a TEM lens operates along the same principles as the lens of a light microscope—the electrons are focused as they pass through the lens and converge to a point on the rear side. This convergence point may also be treated as an object that will be magnified a second time by another lens. A beam of electrons will naturally spread but cannot be focused by an optical lens, so the electron waves must be focused into a beam through the influence of a tunable magnetic field. As the electrons continue through the column, they pass through an aperture, which limits the maximum angle of electron scattering that is transmitted to the sample. They then pass through an electromagnetic focusing lens, which ideally has such a uniform magnetic field that the beam is focused into a perfect circle. The lenses are controlled by varying their current—an increase in current shortens the focal length.[14,15]

Because of the high level of precision required for TEM, any small defect in the focusing magnet will cause astigmatism in the beam. Astigmatism occurs when the right-angle forces on the beam are not even and the focus is distorted into an ellipse. This distortion can be corrected through the use of an octet of smaller electromagnets that surround the outside of the main focusing magnet. The forces can be equalized by adjusting the currents in these magnets, correcting the astigmatism.[14,15]

Ultimately, image formation in a TEM depends on electron scattering. As electrons pass through the sample, they can scatter elastically, scatter inelastically, or pass directly through without being scattered. Elastic scattering occurs when

electrons interact with the sample's atomic nuclei. Inelastic scattering occurs when they interact with electrons in the sample.[14] The difference between scattered and transmitted electrons causes image contrast. The transmitted electrons are viewed on a focusing screen and images are collected with a charge-coupled device (CCD) camera with a computer interface.

Specimen thickness has an effect on the contrast and resolution of an image because thicker specimens have more atomic layers and therefore more opportunities for the electrons to scatter. For samples with nanoscale thickness, depth of field and depth of focus (3900 nm and 2 km for a 100kV scope) are great enough that this thickness is not a limiting factor in imaging, but care must be still taken that the sample thickness is in an appropriate range.[14] Conventionally prepared specimens may be self-supporting or applied to a thin support disk. A TEM grid, 3 mm in diameter and about 50 μm thick, is frequently made of copper, although other materials are available for specialized work. Grids come in different mesh patterns and can be coated with a number of different low-electron-scattering materials (including carbon and polymer films) that support the sample over the holes in the grid and allow electrons to pass through for imaging.[14]

TEM has a number of drawbacks in addition to the restriction of very thin sample thicknesses. TEM is expensive, time-consuming, and limited to examining very small sample sizes.[20] Conventional sample preparation is an *ex situ* technique;[20] biological samples with minimum dimensions greater than 100 nm

[20] Burrows, N. D; Yuwono; V; Penn, R. L. "Quantifying the Kinetics of Crystal Growth by Oriented Aggregation." *Mater. Res. Bull.* **2010**, *35*, 133-137.

must be set in resin and cut into ultrathin slices, a process that requires dehydration and exposure to many different chemicals,[14] while samples prepared by dropcasting are prone to forming artificial aggregates as they dry.[20] One *in situ* technique, cryogenic TEM,[18,20] is examined below. TEM is also limited to producing a two-dimensional representation of a three-dimensional object. Tilting the sample holder to a second angle or using tomography or energy filtering can provide some insight into three-dimensional structure.[20]

There are a few important continuing developments in TEM. One is to further advance high-resolution microscopy, so that a sample's lattice fringes, an indicator of crystallinity, can be seen. At the same time, Müller et al. argue that progress must also be made in sample preparation techniques, particularly in biological fields, if image quality is to continue to improve.[21] A third area of progress is the development and refinement of cryogenic TEM, or cryo-TEM. Cryo-TEM uses samples suspended in a vitrified solution via a flash-freezing process, with the goal of preserving their original three-dimensional arrangement.[18] This rapid cooling vitrifies the solvent and prevents the sample from freezing in a crystalline manner (which would make it visible in a TEM image).[14,18,20] This allows in-situ analysis of particles in suspension[18] and biological specimens in transient conformational states.[21] The mesocrystal intermediate in the transformation of ferrihydrite to goethite is shown in Figure 1, in which the primary particles have aligned themselves in a similar orientation to

[21] Müller, S.A.; Aebi, U.; Engel, A. "What transmission electron microscopes can visualize now and in the future." *J. Struct. Biol.* **163** (2008) 235-245.

the final goethite crystal. They have been vitrified for *in situ* analysis via cryo-TEM.

Preparation of Materials

All glassware and plasticware was acid-washed with 4 M nitric acid prior to use. Labware was then rinsed multiple times with distilled water, followed by multiple rinses with Milli-Q water (Millipore, 18 MΩ·cm resistivity). MilliQ was also used for all solutions and dialysis procedures.

Six-line ferrihydrite was synthesized after Penn et al.[7] Aqueous solutions of 0.4 M ferric nitrate (Fisher) and 0.48 M sodium bicarbonate (Sigma-Aldrich) were prepared. The ferric nitrate solution was heated in a water bath to 45°C and the base was added, while stirring, via peristaltic pump over 11 minutes and 25 seconds. Approximately twelve inches of pump tubing was submerged in the water bath to achieve constant temperature for both solutions. After an additional three minutes of stirring, the blood-red suspension was cooled in an ice bath to 15°C. The suspension was microwaved (Samsung, 950 W) in intervals of 30 seconds with shaking in between until a gentle boil was observed. The microwave anneal step has been found necessary to ensure homogeneous particle size distribution.[9] After microwaving, the suspension was placed in Spectra-Por #7 dialysis bags (MWCO = 2000 g/mol) and refrigerated at 10°C. Samples were stored in the refrigerator (10°C) while being dialyzed against MilliQ water. The water was changed in intervals of at least three hours for a total of nine changes.

After dialysis, a ferrihydrite standard was prepared by diluting 10 mL of the ferrihydrite stock with MilliQ to 100 mL. An additional treatment was prepared by adding 10 mL of 10 mM $FeCl_2$ to 10 mL of ferrihydrite stock and diluting to 100 mL. Likewise, suspensions were prepared with 10 mL of 0.1 mL KH_2PO_4 (Sigma), 0.1 mM alizarin (Acros Organics), and 0.1 mM sucrose (Domino's pure cane sugar). The pH of each of the diluted suspensions was adjusted to 3.71-3.86 with the exception of the sugar-treated suspension, which had a pH of 3.39. The t_0 sample was taken immediately after these suspensions were prepared. The suspensions were then placed in an 80°C oven and 1.5 mL aliquots were removed at intervals of 24±2 hours. The daily samples were stored in a refrigerator at 10°C, which has been found to sufficiently slow growth until characterization.[2]

Characterization

X-ray diffraction

After 23 days, samples were characterized using X-ray diffraction to determine crystal structure and mineral composition. The ferrihydrite suspensions were applied to quartz slides and allowed to dry; multiple layers were deposited. The samples were characterized using a PANalytical X'Pert Pro MPD theta-theta diffractometer with a cobalt source and an X'Celerator detector over the range of 20-90° 2θ. The diffraction patterns were compared to the reference powder diffraction files (PDF) for six-line ferrihydrite (#29-712), goethite (#29-713), and hematite (#33-664).

Transmission electron microscopy

Transmission electron microscopy (TEM) samples were prepared by diluting one drop of suspension into MilliQ water (Millipore). A single drop of the diluted suspension was placed on a 3 mm 200 mesh holey carbon-coated copper grid (Structure Probe, Inc.) and allowed to air dry. Grid preparation began within two weeks of the initial sampling date. Calibrated images were taken with an FEI Tecnai T12 microscope, operated at 120 kV, or an FEI Tecnai F30 microscope, operated at 300 kV. Images were collected using a Gatan charge-coupled device (CCD) camera and processed with Gatan Digital Micrograph 3.8.2. Measurements were performed using ImageJ 1.40g, a public domain NIH image processing and analysis software written by W. S. Rasband.

The average volume of time zero (immediately post-dialysis, three days post-synthesis) ferrihydrite particles was determined measuring the length of 500 particles, assuming a 1.3 aspect ratio,[2,7,22] and calculating volume based on an ellipsoidal shape.[2,22] The volume calculations for the alizarin-treated samples followed the same procedure; 417-810 particles were measured for each of the selected sample days. The rate of dot-to-rod conversion was quantified by first taking volume measurements of all whole goethite rods seen in the TEM images. The volume of the rods was divided by the average volume of a t_0 ferrihydrite particle to determine the number of primary particles required to produce the rods. The concentration of the remaining primary particles was calculated according to the equation

[22] Jentzsch, T. L; Penn, R. L. Influence of Aluminum Doping on Ferrihydrite Nanoparticle Reactivity. *J. Phys. Chem. B* **2006,** *110,* 11746-11750.

$$[P] = \frac{\#P_{dots}}{\#P_{total}} \cdot [P_0]$$

where $\#P_{dots}$ is number of ferrihydrite dots counted in the images, $\#P_{total}$ is the number of dots counted plus the number of dots required to produce the measured volume of goethite rods, and $[P_0]$ is the initial concentration of the ferrihydrite suspension. The rate constant, *k*, was determined from a plot of 1/[P] vs. time, consistent with second order kinetics.

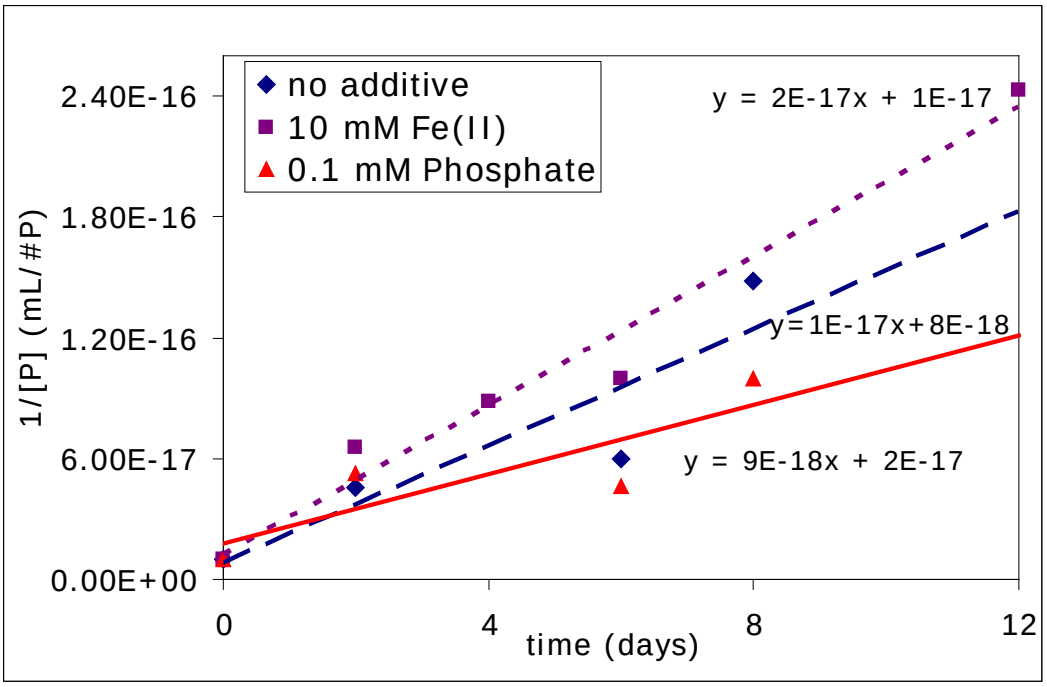

Figure 4: Rate of phase transformation from ferrihydrite to goethite, assuming rapid equilibrium and a second-order rate law.

Results and Discussion

The addition of surface-active chemical species to ferrihydrite suspensions prior to aging had an effect on both the rate of ferrihydrite transformation and the resultant product. When assuming rapid equilibrium, the growth follows a second-order rate law and can be quantified from a graph of the inverse of primary

particle concentration versus time, as shown in Figure 4. The rate constant *k*, the slope of the graph, has uncertainty due to non-ideal fit for the linear regression equation. Figures 5-7 are plots of 1/[P] vs. time for the untreated sample and the samples treated with 0.1 mM phosphate and 10 mM Fe(II), accompanied by a TEM image for each sample after six days at 80°C. For the untreated ferrihydrite sample (Figure 5), the rate constant *k* was found to be 1.5×10^{-17} mL/#P·days. XRD of a sample aged for 23 days confirms that the only iron oxide species present are ferrihydrite and goethite. The XRD of all samples are displayed in Figure 8.

Growth slowed in the sample with phosphate to a rate of $k=8.6 \times 10^{-18}$ mL/#P·days (Figure 6). XRD shows that this sample contained ferrihydrite and goethite, while TEM show that the goethite rods are all in sizes and aspect ratios typical of a pure ferrihydrite/goethite system. The decrease in growth rate with the addition of a foreign species seems to be a reasonable extrapolation from the process of secondary structure formation, which requires that any solvent molecules on the particle surfaces be removed or internally incorporated into the new crystal.[5,11] However, the growth rate did not always decrease.

The addition of Fe(II) to the suspension increased the rate of growth to $k=1.9 \times 10^{-17}$ mL/#P·days (Figure 7). TEM images show rods in a bimodal distribution of aspect ratios, with a significant population of rods that are wider than those seen in an untreated ferrihydrite/goethite suspension. The iron oxide species in this sample are also limited to ferrihydrite and goethite.

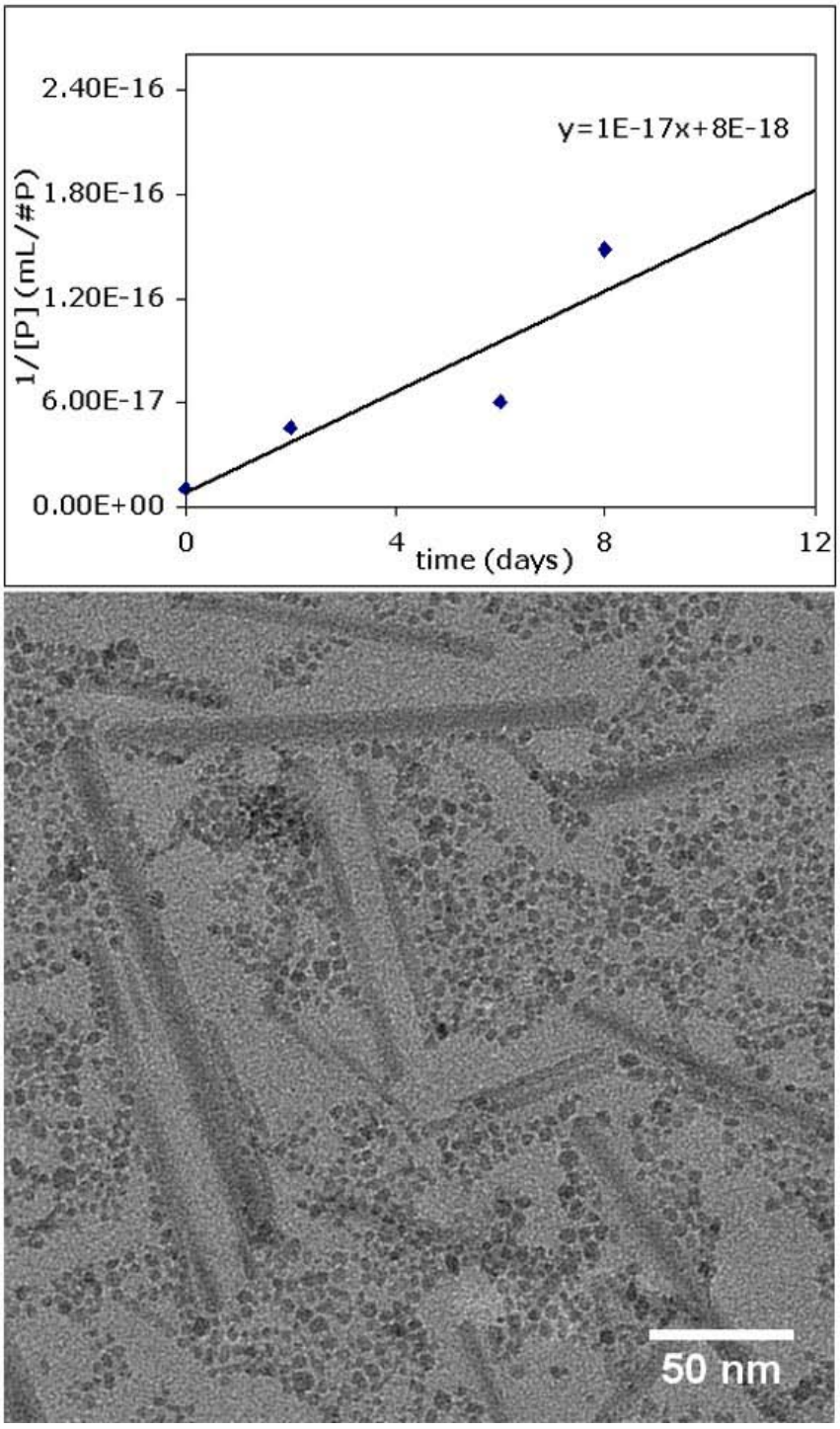

Figure 5: Ferrihydrite with no added surface-active species. A plot of 1/[P] vs. time (top) and a transmission electron micrograph (bottom) of a sample after six days of aging at 80°C.

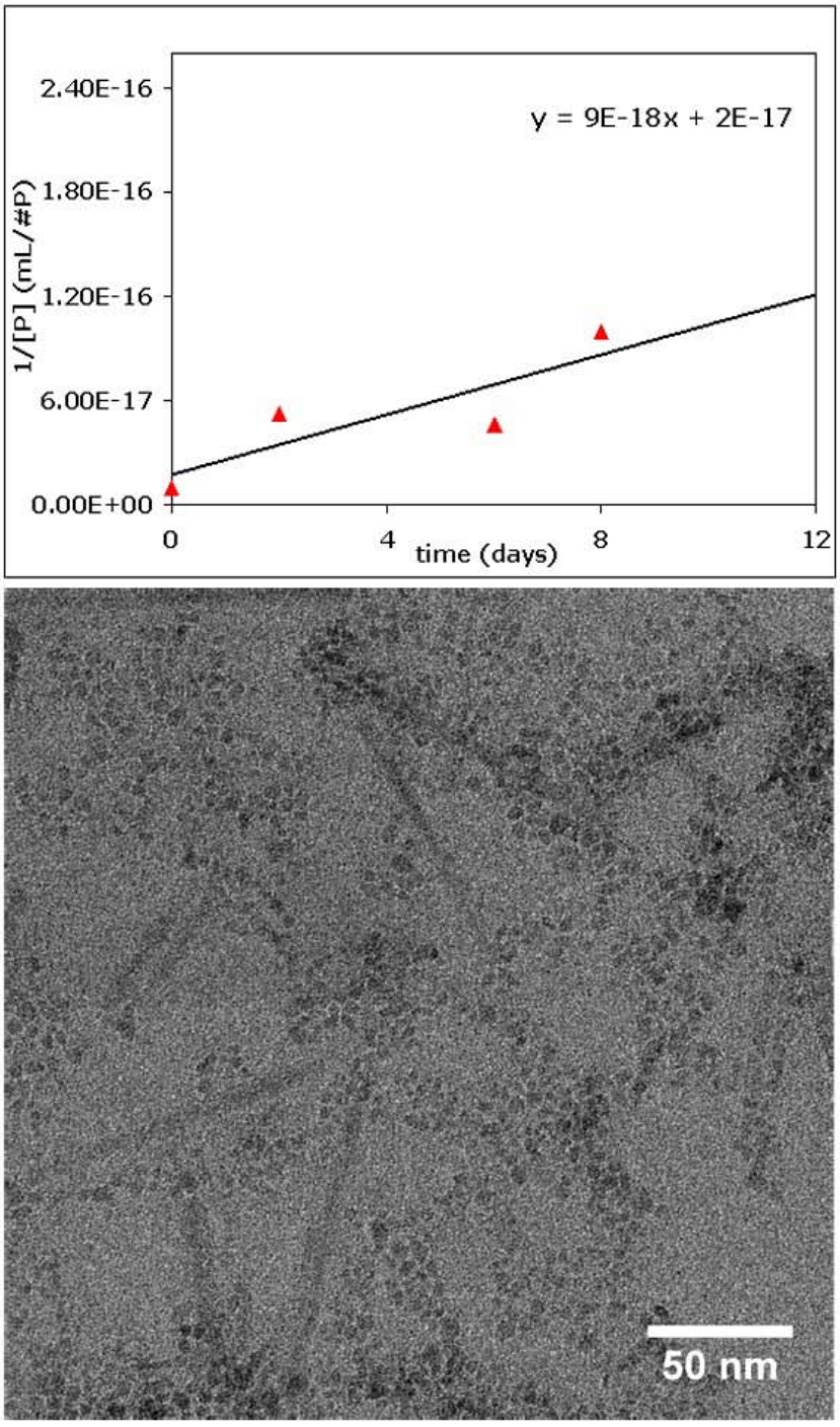

Figure 6: The sample treated with 0.1 mM phosphate exhibits a decreased growth rate (top). After six days of aging at 80°C, goethite rods are present alongside ferrihydrite dots (bottom).

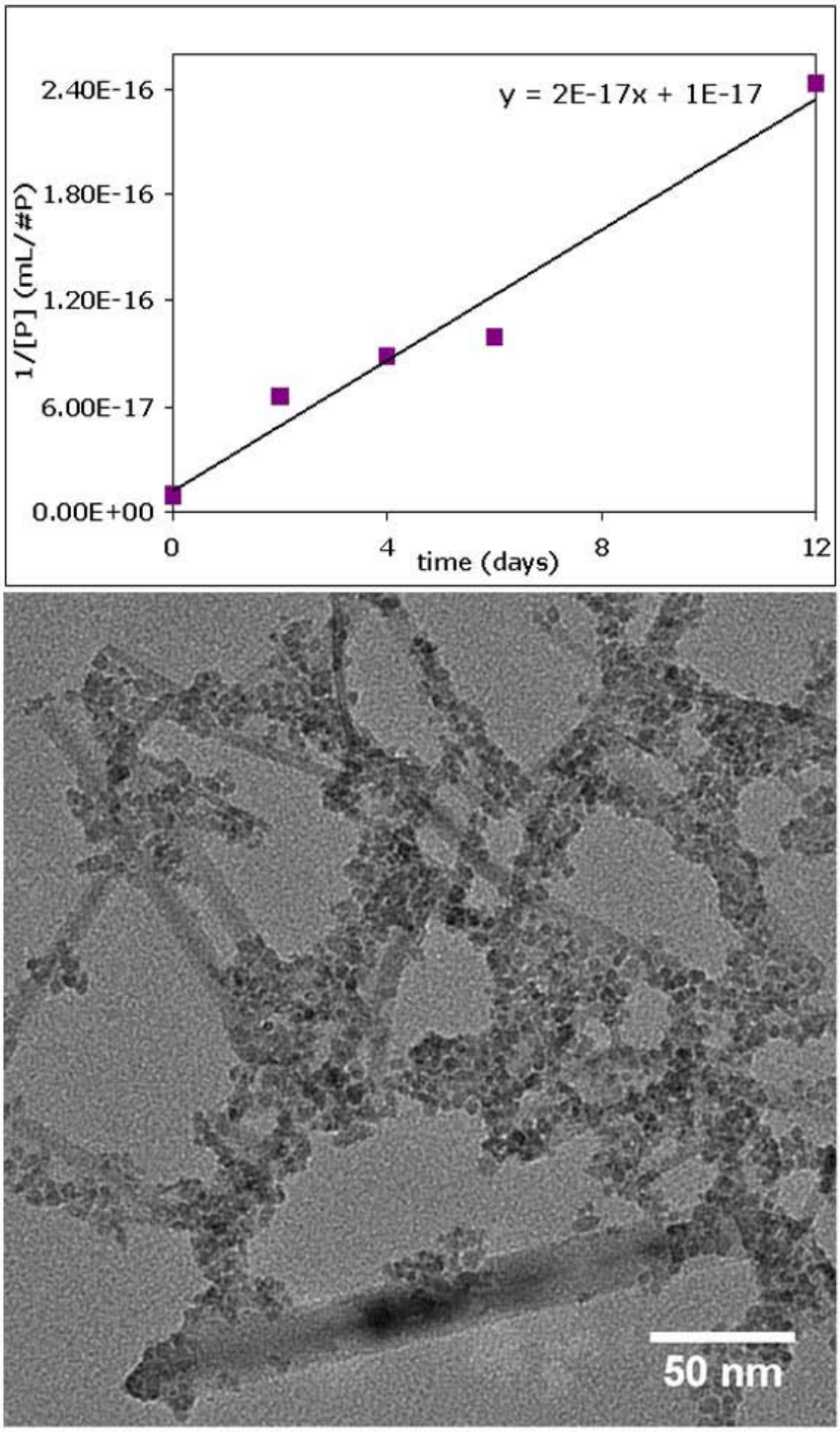

Figure 7: The Fe(II)-treated sample had an increased rate of conversion from dots to rods relative to that of the untreated ferrihydrite sample (top). The transmission electron micrograph (bottom) shows a bimodal distribution of rod aspect ratios after six days of aging at 80°C.

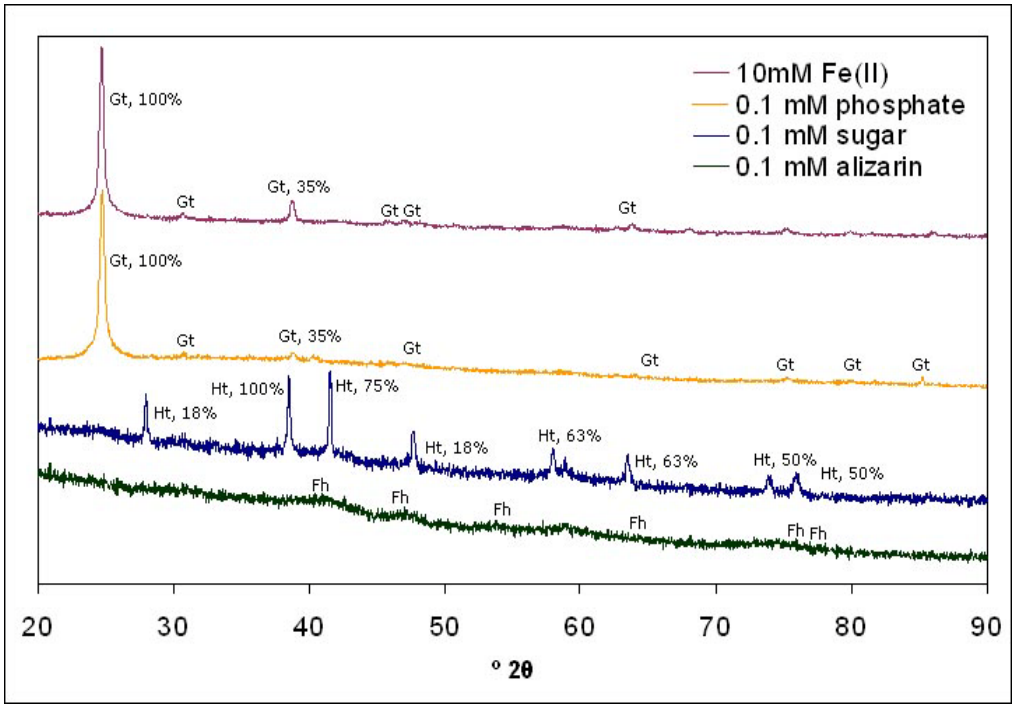

Figure 8: XRD of untreated ferrihydrite suspension and samples treated with phosphate, sugar, and alizarin, aged for 23 days at 80°C. The diffractograms have been offset for clarity.

When sugar was added, an additional iron oxide species was formed. XRD and TEM both show the presence of hematite in addition to ferrihydrite and goethite. Figure 9 shows two TEM images of irregularly shaped hematite crystals from a sugar-treated ferrihydrite suspension aged 20 days. The lattice fringes are clearly present in the high-resolution image, indicating a crystalline substance. Sugar also affected the morphology of the goethite rods: some are the expected flat-edged structures, but kayak-shaped rods with bowed sides were also formed. An example of these curved rods is shown in Figure 10. Due to the presence of hematite and the curved rods, no attempt was made to quantify the rate of transformation from ferrihydrite.

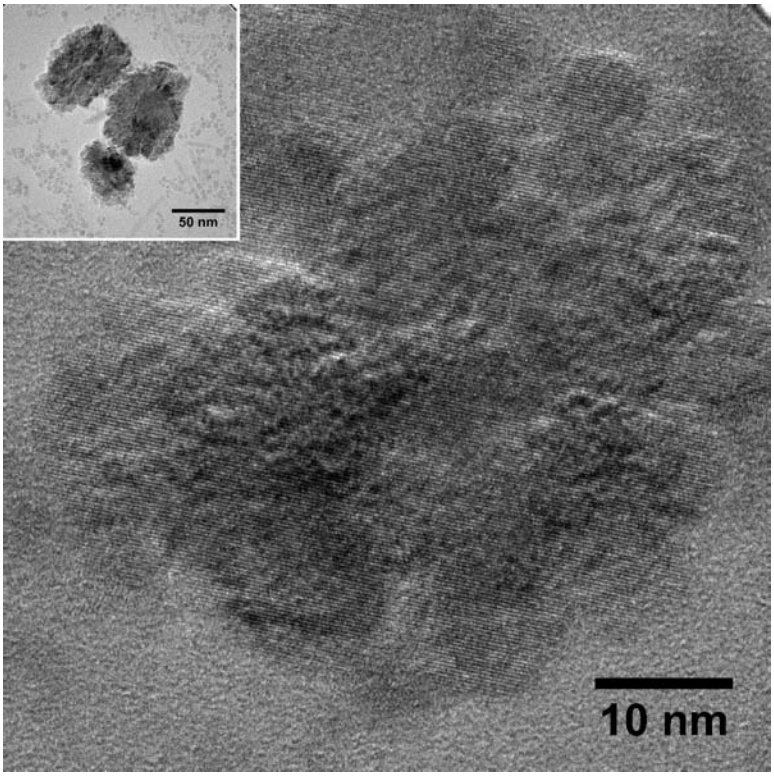

Figure 9: A high-resolution transmission electron micrograph of an irregularly shaped hematite crystal from a ferrihydrite sample treated with 0.1 mM sugar and aged for 20 days at 80°C. The inset (scale bar 50 nm) shows three hematite crystals in the presence of ferrihydrite nanoparticles and goethite nanorods. The lattice fringes are visible in the hematite crystal, indicating a high degree of crystallinity.

The addition of alizarin, a catechol chosen for its multiple binding sites, prevented transformation of ferrihydrite into goethite even after aging at 80°C. XRD at 23 days (Figure 8) shows only ferrihydrite peaks. After 36 days, only 1.2% of the total volume of primary particles had converted to goethite rods. In comparison, the ferrihydrite sample with no additive had a conversion of 72.0% of the total dot volume into goethite after only eight days. A TEM image of the alizarin-treated sample after 33 days of aging is displayed in Figure 11.

Measurement from TEM shows the average size of the alizarin-treated particles increased from 4.5±1.0 nm to 4.9±1.0 nm. The data for alizarin growth

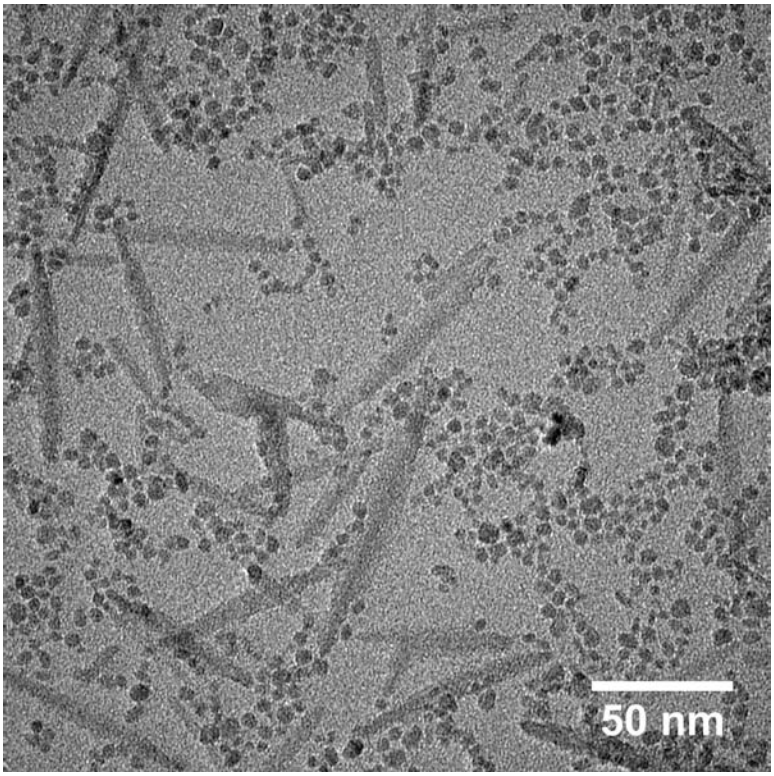

Figure 10: Ferrihydrite sample treated with 0.1 mM sugar and aged 20 days at 80°C. Ferrihydrite particles and kayak-shaped goethite rods dominate this image.

are displayed in Table 1 and graphed as a function of average size vs. time in Figure 12. Although the oldest particles are larger than the youngest ones, the largest average sizes come from a number of intermediate data points. This lack of a clear, positive growth trend does not support the hypothesis that alizarin-treated dots will significantly increase in size; XRD and TEM, however, did confirm that the alizarin-treated sample could be aged for at least 36 days without very many particles transforming into goethite. Additionally, a probability-normalized histogram (bin size of 0.5 nm), as shown in Figure 13, of alizarin particle lengths shows a slight shift in the mode over time. The scattering of data points in Figure 12 reflects an inconsistency in size measurements likely explained by human error. The TEM images were not taken at a consistent

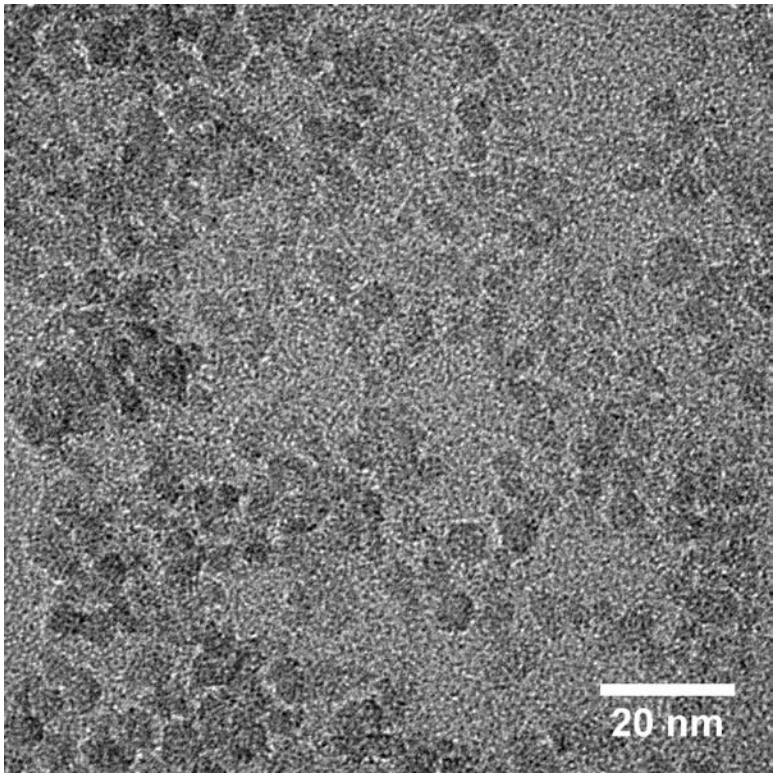

Figure 11: After 33 days, the alizarin-treated sample is still mostly ferrihydrite.

Day	Number of dots	Average length (nm)	Std. dev. (nm)
0	417	4.5	1.0
2	820	4.8	0.90
4	800	4.9	1.0
8	611	4.7	1.0
20	464	4.8	1.1
33	610	4.6	0.84
36	810	4.9	1.0

Table 1: Change in average length of alizarin-treated ferrihydrite nanoparticles.

resolution across the different sampling days and the images for some times (notably days 2 and 4) were mostly lower-resolution images, with the majority of micrographs at resolutions of 2.2 pixels/nm. The samples from days 8 and 36 had

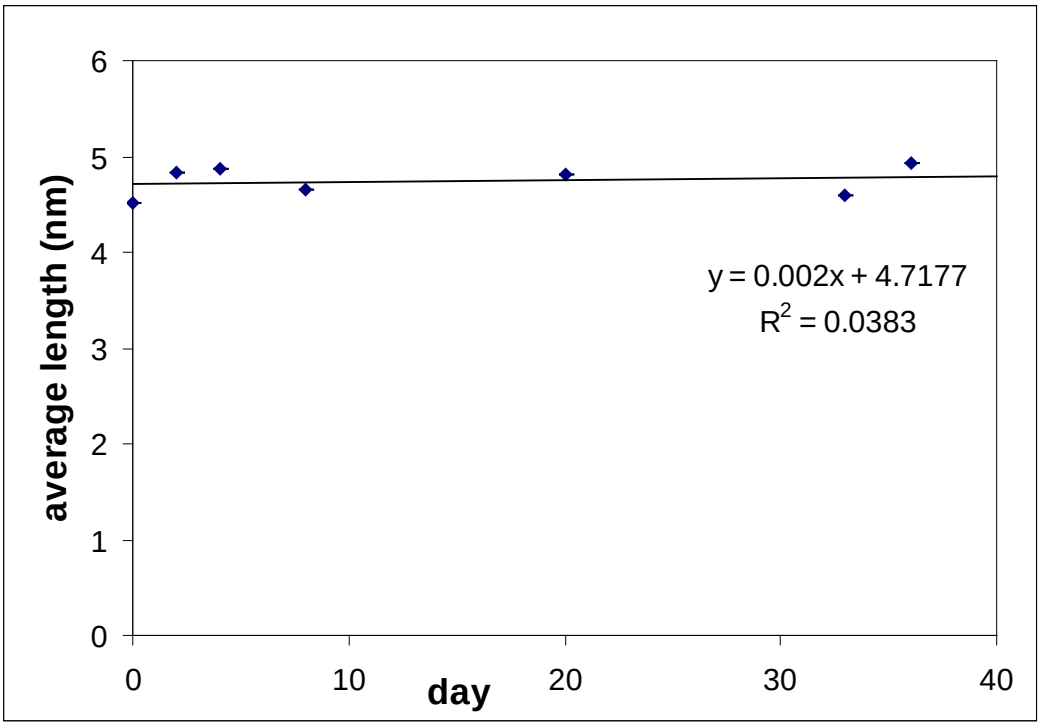

Figure 12: The change in average length of alizarin-treated particles over time.

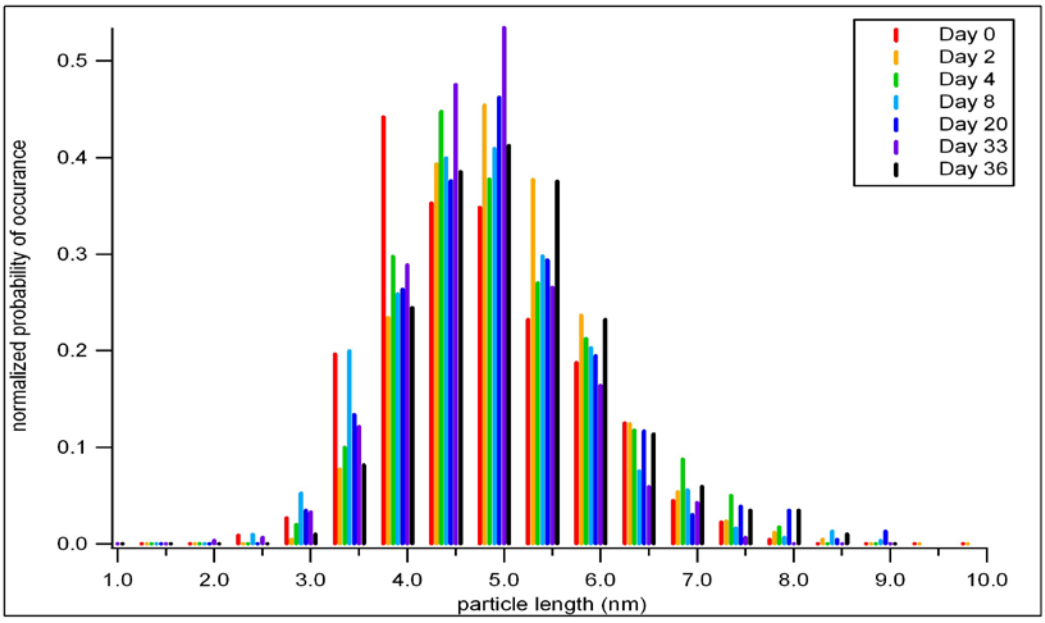

Figure 13: Histogram of alizarin-treated particle lengths with frequency of occurrence normalized. Bin size of 0.5 nm.

the next-lowest resolution images (2.7-5.9 pixels/nm), while days 0, 20, and 33 ranged in resolution from 7.1-27.9 pixels/nm. The low resolution of some of these images makes it difficult to precisely measure the length of such small objects. The images with lower resolution are prone to over-measuring because of the difficulty in pinpointing the edge of the particles.

Conclusion

The addition of surface-active chemical species to ferrihydrite suspensions prior to aging affected their subsequent growth and transformation in a number of ways. The addition of phosphate caused the rate of ferrihydrite to goethite transformation to slow but had no effect on the presence of other iron oxide species. When Fe(II) was added, not only did the rate of dot-to-rod transformation increase, the rod morphology also changed, with rods of both very narrow and very wide widths visible. Sugar affected rod morphology and the kinds of iron oxides produced; transformation rate was not quantified. In the sugar-treated sample, flat- and bowed-edged (kayak shaped) goethite rods are present, as are irregularly shaped hematite crystals. Finally, the alizarin-treated sample had a dramatic decrease in the rate of transformation from ferrihydrite to goethite, with conversion almost completely stopping. A handful of goethite rods (1.2% by volume after 36 days) are visible in the TEM from this sample but did not register on the XRD.

Chapter 2: A Survey of TOPO-Capped Silver Nanoparticle Films

Introduction

Research in nanoparticle and quantum dot (QD) chemistry has rapidly progressed over the last 25 years.[1] Semiconducting QDs exhibit tunable size-dependent emission, high photoluminescence yields, broad excitation spectra, and narrow emission bandwidths.[2] Quantum dots have applications in thin-film light-emitting diodes,[2] biological labels,[2] biosensors,[1] photodetectors,[1] Förster resonant energy transfer (FRET) sensing,[1] and nanoscale optics and switches,[3] but it should be noted that many of these applications require some degree of quantum dot assembly.[1] Water-soluble particles can be arranged via conventional techniques such as layer-by-layer (LbL) or spin-assisted LbL assembly, but hydrophobic particles are more favorably manipulated at the air-water interface.[1]

One such approach is thin-film assembly via Langmuir-Blodgett (LB) and Langmuir-Schaefer (LS) mono- and multi-layers of organized QD/nanoparticle systems. After dispersal on a water surface, particles are vertically (LB) or

---

[1] Lambert, K; Čapek, R. K; Bodnarchuk, M. I.; Kovalenko, M. V; Van Thourhout, D; Heiss, W; Hens, Z. "Langmuir-Schaefer Deposition of Quantum Dot Multilayers." *Langmuir*. **Article ASAP**. Web publication February 3, 2010.

[2] Ji, X; Wang, C; Xu, J; Zheng, J; Gattá-Asfura, K. M; Leblanc, R. M. "Surface Chemistry Studies of (CdSe)ZnS Quantum Dots at the Air-Water Interface." *Langmuir* **2005**, *21*, 5377-5382.

[3] Tatewaki, Y; Noda, Y; Akutagawa, T; Tunashima, R; Nori, S; Nakamura, T; Hasegawa, H; Mashiko, S; Becher, J. "Langmuir-Blodgett Films Constructed from a Charge-Transfer Complex and Gold Nanoparticles." *J. Phys. Chem. C* **2007**, *111*, 18871-18877.

horizontally (LS) deposited onto a substrate.[1,4] Particle packing and arrangement is greatly influenced by particle size, shape, and capping ligand.[4] Metal nanoparticles are susceptible to re-aggregation into bulk material without an appropriate covering material.[5,6] This study investigates the arrangement of three sizes of trioctylphosphine oxide (TOPO)-capped silver nanoparticles when deposited as Langmuir-Schaefer films at a variety of compression levels.

The use of Langmuir-Blodgett and Langmuir-Schaefer techniques is significant because they enable the bottom-up creation of monolayer films of nanoscale materials—including capped nanoparticles and quantum dots—packed over a large area.[4] One particular advantage that this technique offers is the ability to adjust macroscopic properties (such as surface pressure) to control nanoscale assembly.[4] As a result, mono- and multi-layer semiconducting films can be created using the tunability of the film manufacture process to control particle packing. Langmuir-Blodgettry can also be used to study the surface chemistry properties of quantum dots that imitate biological interfaces,[4,5] combined with layer-by-layer assembly for microcontact printing and micropatterning,[1] or used for forming organic films of aromatic compounds, dyes, porphyrins, long-chain aliphatic compounds, and various biological molecules.[4]

The conductivity of semiconducting particle films is affected by the film structure and molecular packing in a number of ways. One barrier to conductivity

---

[4] Tao, A. R; Huang, J; and Yang, P. "Langmuir-Blodgettry of Nanocrystals and Nanowires." *Acc. Chem. Res.* **2008**, *41*, 1662-1673.
[5] Saponjic, Z. V; Csencsits, R; Rajh, T; Dimitrijevic, N. M. "Self-Assembly of TOPO-Derivatized Silver nanoparticles into Multilayered Film." *Chem. Mater.* **2003**, *15*, 4521-4526.
[6] Wang, Z. L, Ed. *Characterization of Nanophase Materials*. Wiley-VCH: New York, 2000. 406 pp.

is the granular structure of the films and the structure of the particles themselves. Intergrain barriers to conduction exist in part because of the nonconducting capping materials that are commonly applied to the particles. The general structures of the films have areas of ordered packing separated by areas of disordered packing. Electron transport is difficult or impossible through the disordered domain barriers. This particularly limits conductivity through a monolayer, where there are few alternate conduction pathways. In a three-dimensional crystal, defects can be circumvented by pathways that avoid the disordered regions, but this is not possible in a single layer of molecules. The conductivity of multilayer films lies somewhere in between, but in a multilayer film of capped particles, there is also a greater amount of capping material between the semiconducting components, which increases the activation barrier.[7]

Whether a monolayer or a multilayer is formed, nanoparticle assemblies often include some kind of capping material or core-shell structure to prevent particle aggregation. The ideal capping material, often a ligand, permits interparticle assembly while simultaneously allowing the repulsive forces between the nanoparticles to prevail over interparticle aggregation. It must also uniformly coat the particle and must not interfere with or modify any of its structural and electronic characteristics. Without a capping shell capable of preventing aggregation, the particles would irreversibly re-aggregate and the novel optical and electronic properties they possessed as nanoparticles would be lost. In

[7] Talham, Daniel R.. "Conducting and Magnetic Langmuir-Blodgett Films." *Chem. Rev.* **2004**, *104*, 5488.

particular, pure silver nanoparticles, when clumped, exhibit all of the properties of bulk silver metal.[5]

A number of capping ligands for gold and silver nanoparticles have been studied, including organic alkanethiol-functionalized ligands and quaternary amines, as well as particles such as SiO_2-capped gold ($Au@SiO_2$), which have metal cores and optically transparent inorganic shells, where the shell works analogously to the cap in preventing aggregation. The long, ordered alkane chains of many organic ligands are favorable because they encourage spontaneous assembly and control interparticle spacing. Each ligand has an inorganic component, such as the dithiol and amino groups in the ligands mentioned here, that links the ligand to the particle. The covalent metal-sulfur bonding between alkanethiols and gold and silver particles makes thiol-capped molecules particularly stable, but the formation of a semiconducting AuS_2 or AgS_2 layer changes the electronic properties of the particles. This makes thiols undesirable capping ligands for any investigation of electronic properties in metal nanoparticles.[4,5]

Tri-*n*-octylphosphine oxide (TOPO, Figure 14) has been reported as an ideal ligand for investigations the behavior of semiconducting nanoparticles.[2,7] TOPO has three long alkane chains that encourage self-assembly of particles and a phosphine oxide group that binds to the metal surface. The oxygen atom causes TOPO to be a strongly coordinating ligand.[8] The large dipole moment of the

[8] Hąc-Wydro, K.; Wydro, P.; Dynarowicz-Łątka, P. "A study of the interaction between dialkyldimethylammonium bromides and tri-*n*-octylphosphine oxide (topo) in mixed monolayers at the air/water interface." *Journal of Colloid and Interface Science*. **2004.** *278*, 206.

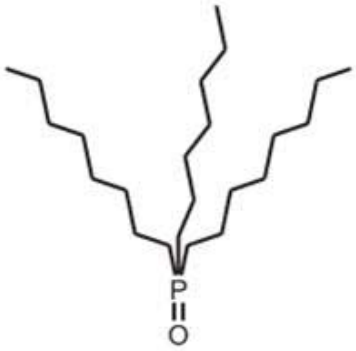

Figure 14: Tri-*n*-octylphosphine oxide (TOPO).

phosphorous-oxygen bond permits TOPO-capped quantum dots to form a stable monolayer at an air-water interface.[2] Additionally, the electrostatic interactions of the alkyl chains help prevent particle agglomeration.[5] The nonpolar nature of the alkyl chains also makes TOPO soluble in nonpolar solvents such as chloroform, hexane, cyclohexane, and toluene.[5,7] Benzene is the only solvent that can penetrate between the chains, while polar solvents (water, alcohol) have very little interaction with the particles and cannot wet the film.[5] In the case of a nonpolar colloidal solution, the immiscibility of the solvent with water enables it to be suspended on the surface of a water layer. The particles can then be deposited onto a solid substrate to make single- or multi-layer films. The immiscibility of the particle suspension with the subphase is an essential part of the Langmuir-Blodgett and Langmuir-Schaefer techniques. Films made from these solutions can be redissolved in organic solvents without any aggregation.[8]

The in-situ formation of self-assembled multilayer films onto glass slides during late-stage TOPO-capped Ag particle synthesis has been reported.[5] Single layer films of TOPO-Ag particles, as well as other TOPO-capped particles, such

as (CdSe)ZnS core-shell quantum dots, have been formed using the Langmuir-Blodgett technique.[7] The spacing between particles in these monolayers is of interest because interparticle coupling is primarily controlled by particle size and interparticle separation.[5] Changing the particle size affects the amount of capping molecules between the particles, while changing the surface pressure of the particle layer before a Langmuir deposition alters the spacing of the particles. This is significant when using a system of conducting particles because the dielectric property of an individual particle is changed by the presence of closely-packed adjacent particles.[7]

The monolayer preparation process faces a number of challenges. When using Langmuir techniques, film transfer from water surface to substrate depends on the adhesion of the surfactant to the substrate, which itself depends on the hydrophobicity of the surfactant relative to the substrate and the water surface. Once touching, particles begin to aggregate, causing clumps in the monolayer or regions of multilayer films.[1]

This project examines the packing of TOPO-capped Ag nanoparticles when manufactured as Langmuir-Schaefer monolayers, as characterized through atomic force microscopy. The goal of this project was to characterize TOPO-capped Ag nanoparticle monolayers for a variety of particle sizes at different synthesis surface pressures and use them as a model system for microscopic characterization of nanoparticle films.

Experimental

Langmuir Films

Langmuir films are made using an instrument called a Langmuir or Langmuir-Blodgett trough, shown in Figure 15. The basic architecture of the instrument consists of a shallow trough filled with water, with one deeper cavity into which the substrate can be dipped. A mechanical arm protrudes over the surface of the water; a clip on the end of the arm allows it to control the dipping rate and position of the solid substrate. A set of movable barriers is electronically controlled to skim the surface of the water, compressing any molecules that are floating on that surface. A strip of paper called a Wilhelmy plate hangs into the water and measures surface pressure. The plate is suspended from a sensitive balance, which measures the net downward force composed of the downward forces of gravity and surface tension on the plate and the upward force due to buoyancy. For a rectangular plate with density ρ_w and dimensions *w*, *t*, and *l*, immersed to a depth *h* in a liquid with density ρ_L,

$$F = \rho_w glwt + 2\gamma(t + w)\cos\theta - \rho_L gtwh$$

where γ is the surface tension of the liquid, θ is the contact angle between the water surface and the plate, and *g* is the gravitational constant. When the plate is very thin ($t << w$), the change in surface pressures ($\Delta\gamma$) is equal to one half the change in force divided by the width of the plate: [9]

$$\Delta\gamma = \frac{\Delta F}{2w}$$

[9] Petty, Michael C. *Langmuir-Blodgett films: An introduction*. Cambridge: Cambridge University Press, 1996. 53-54.

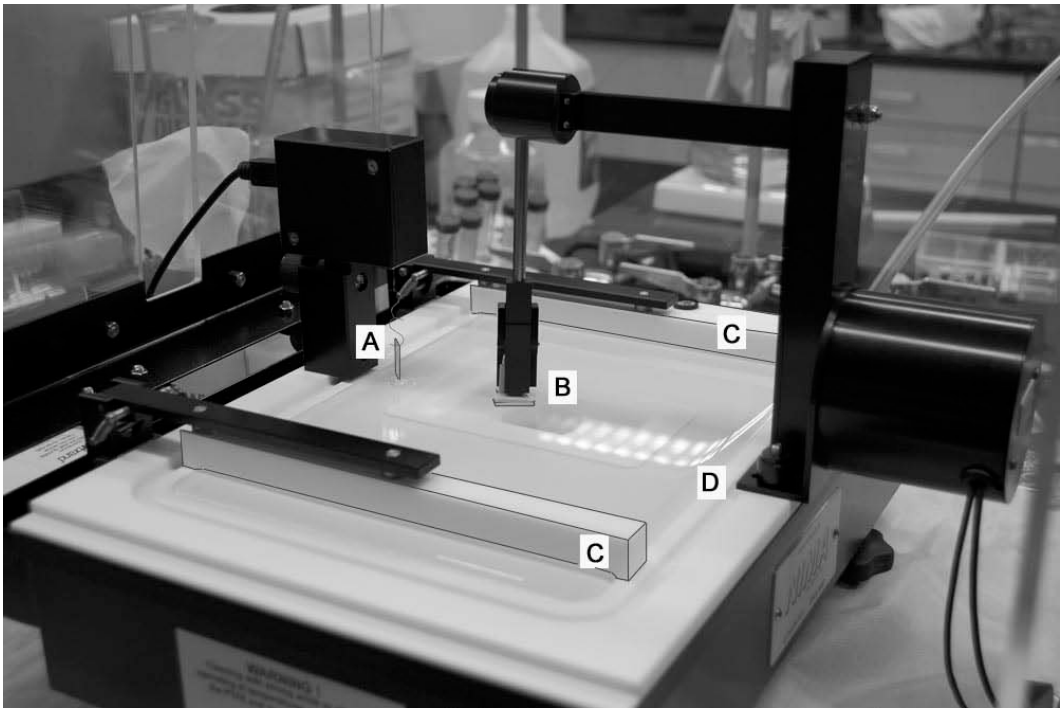

Figure 15: A Langmuir-Blodgett trough with major parts labeled. (A) Wilhelmy plate, (B) substrate clamped into dipping mechanism, set up for horizontal dipping, (C) compression barriers, and (D) water surface. Trough shown is a NimaPro Nima516 LB Trough, manufactured by Nima Technology Ltd.

A Langmuir film is made of a hydrophilic or hydrophobic molecular surfactant and a corresponding highly hydrophilic or hydrophobic solid substrate. The surfactant is suspended in a volatile solvent, such as chloroform, and then carefully dropped onto the surface of the water subphase. After a period of evaporation, all that remains is a disperse, disordered layer of surfactant molecules floating on the water surface. The barriers are moved to compress the surfactant molecules to the desired surface pressure, at which point the substrate is raised or lowered through the surface of the water. During the compression process, a pressure vs. surface area isotherm (Figures 16 and 17) is recorded. The isotherm demonstrates how surface pressure increases as area decreases and

provides an insight into the relative closeness of particle packing and the extent of particle interactions. Figure 16 shows an isotherm for heptadecanoic acid (HDA) on a water subphase. The HDA isotherm has distinct inflection points as the system passes through a series of physical phases.

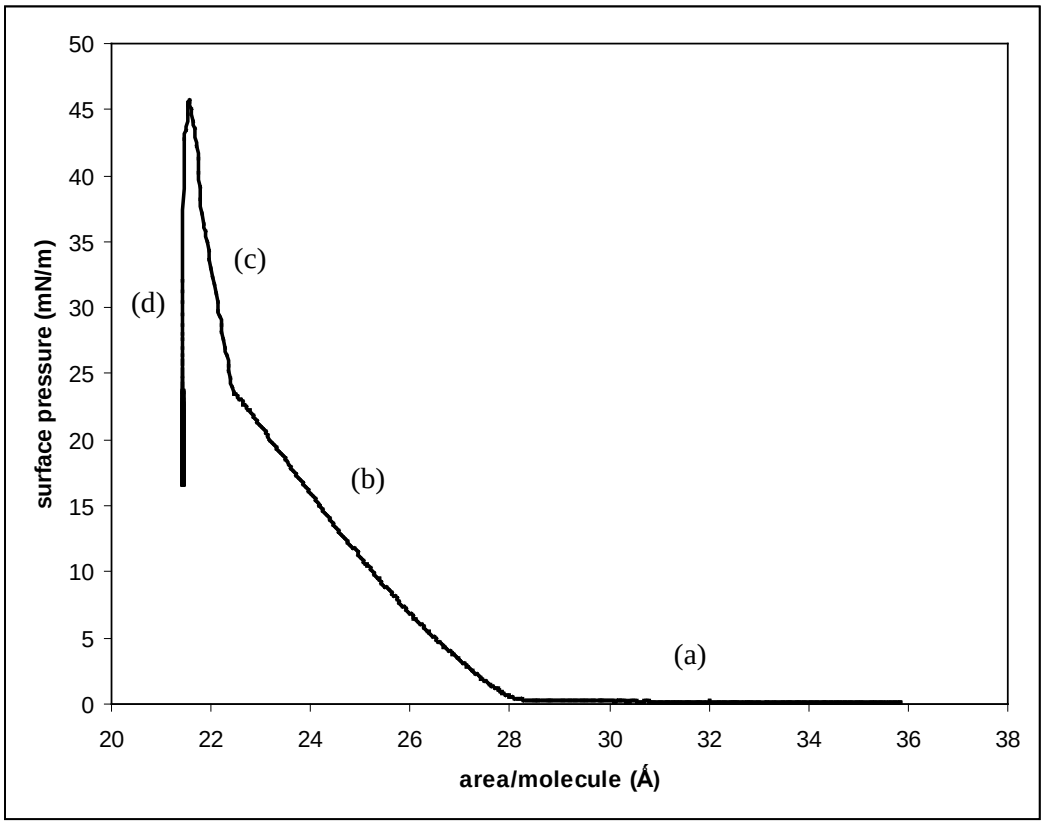

Figure 16: Pressure vs. area isotherm of heptadecanoic acid compressed from (a) gas phase to (b) liquid-expanded and (c) liquid-condensed phases. (d) shows the collapse of surface pressure as deposition occurs and the substrate is raised through the surface of the film.

The construction of a Langmuir film begins with a single layer of surfactant molecules widely dispersed on the surface of an aqueous subphase. At this point, the molecules are spread so far that they have no interaction with each other and no contribution to the surface potential of the subphase.[5] This state is

described as a two-dimensional gas phase, analogous to the gas phase of a three-dimensional system (Figure 16a).[5]

As compression continues, the surface area per molecule decreases and the molecules are more closely arranged. In the liquid-expanded phase, the two-dimensional equivalent of the ordinary liquid state, the surfactant molecules begin to interact with one another (Figure 16b).

In the liquid-condensed phase, the two-dimensional phase that corresponds to the three-dimensional solid phase, the molecules are most closely packed while still arranged as a single layer (Figure 16c). This layer is not necessarily a true 2-D solid, but does have short-range structural coherence. Any further pressure increase beyond this point will cause the layer to collapse, either with the shearing of the layer as it slides over itself, or with the folding over of the layer into the subphase. The surface pressure also drops as the monolayer collapses when deposition onto a substrate occurs (Figure 16d).

The phase changes of the film system are monitored as a function of surface pressure, which is measured by the Wilhelmy plate and defined as the difference in surface tension of the monolayer (γ) and that of the pure subphase (γ_0), $\Pi = \gamma - \gamma_0$.[5,7] The isotherm displays the change in surface pressure as the barriers compress. For some species, such as heptadecanoic acid, the slope of the isotherm changes distinctly at each phase change. In others, as seen in the isotherm for TOPO-capped silver particles, the change of slope is gradual over the entire compression area (Figure 17). Manipulating the surface pressure changes the particle density on the water subphase and directly affects particle

arrangement in the finished film. The shape of the isotherm and the arrangement of particles in the monolayer is compound-specific

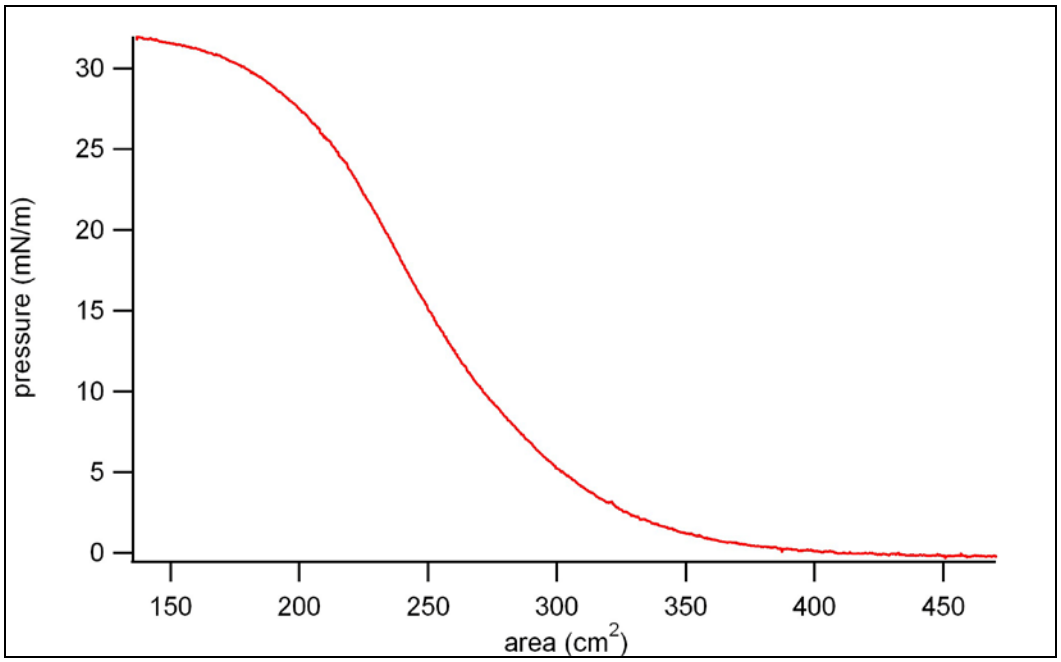

Figure 17: Pressure vs. surface area isotherm for 30 nm TOPO-capped silver nanoparticles compressed to 32 mN/m.

There are two methods of depositing particles onto the substrates, forming Langmuir-Blodgett and Langmuir-Schaefer films. The difference between these deposition techniques is illustrated in Figure 18. To produce a Langmuir-Blodgett monolayer (Figure 18a), a hydrophilic substrate is lowered into the water before the surfactant, dissolved in a solvent like chloroform, is spread onto the water surface. The solvent is then allowed to evaporate, the barriers are compressed, and the substrate is raised, depositing the monolayer. For a hydrophobic substrate, the surfactant is first spread over the water and the substrate is then lowered through the surface. The dipping procedure may be repeated as many times as desired to form a multilayered film. Films formed by vertical dipping of the substrate, the

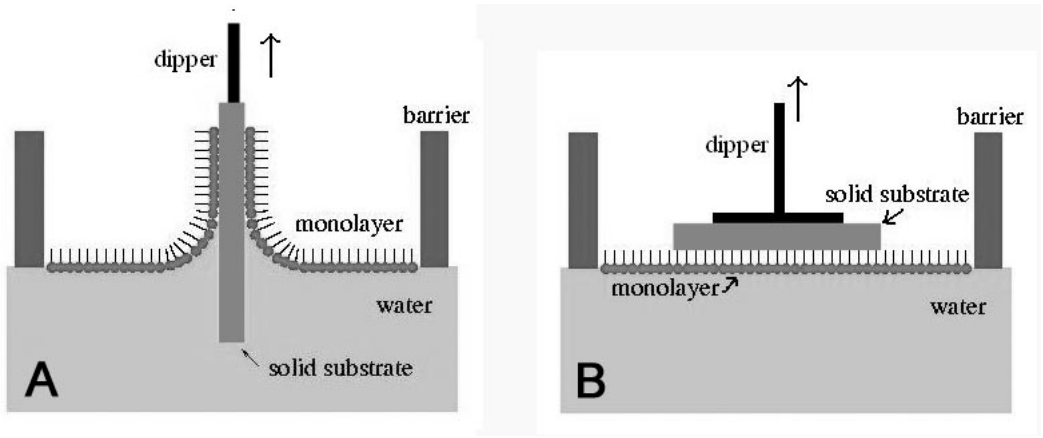

Figure 18: In a Langmuir-Blodgett deposition (A), the substrate is held perpendicular to the water surface. This is an example of a hydrophilic substrate. In a Langmuir-Schaefer deposition (B), the substrate is positioned parallel to the water surface.

most common method of deposition, are referred to as Langmuir-Blodgett (LB) films. In the case of a Langmuir-Schaefer (LS) film (Figure 18b), the substrate is mounted horizontally and then lifted through the layer or touched gently to the water surface.[7] The samples presented in this project were prepared exclusively using LS technique.

Although Langmuir-Blodgettry is an excellent method for producing single-layer films, the molecular arrangement of the finished film is not guaranteed. A surface pressure vs. area (π-A) or surface potential vs. area isotherm shows that a monolayer has formed on the water surface, but does not guarantee that the monolayer is successfully transferred to the substrate.[5] A variety of analysis techniques may be applied to determine film composition and structure. These include, but are not limited to, the use of atomic force and scanning electron microscopies for imaging particle packing. Transmission

electron microscopy (TEM) can also be performed on films that have been prepared directly on TEM grids.

Atomic Force Microscopy

Atomic force microscopy (AFM) can be used to examine the surface topography of a range of substances, with applications in polymeric biomaterials,[10] metals, semiconductors, organic layered systems,[6] and Langmuir-Blodgett monolayers such as those described here. Additionally, a recent paper describes the use of AFM to detect cancer cells based on the difference in rigidity between cancerous and non-cancerous cells.[11] The atomic force microscope, developed in 1986 by Gerd Binnig, Calvin Quate, and Christoph Gerber (Binnig, along with Heinrich Rohrer, was awarded the 1986 Nobel Prize in Physics for the invention of a related instrument, the scanning tunneling microscope),[12] is part of a family of microscopy techniques that all fall into the category of scanning probe microscopy.[6,10] Scanning probe microscopes can be adjusted to analyze electronic energy specra,[6] local elasticity,[6] and local magnetic and electrostatic properties,[6] as well as used as a tool for nano-lithography.[6,13]

AFM works by using sharp probe, often made of doped silicon, to scan over the surface of a sample. Scanning is controlled through the relative

---

[10] Merrett, K; Corneilius, R. M; McClung, W. G; Unsworth, L. D; Sheardown, H. "Surface analysis methods for characterizing polymeric biomaterials." *J. Biomater. Sci. Polymer Edn.* **2002**, *13*, 593-621.
[11] Cross, S. E; Jin, Y-S; Rao, J; Gimzewski, J. K. "Applicability of AFM in cancer detection." *Nat. Nanotechnol.* **2009**, *4*, 72-73.
[12] "Scanning Probe Microscopy Training Notebook." Version 3.0. Digital Instruments, Veeco Metrology Group, 2000.
[13] Prime, D; Paul, S; Pearson, C; Green, M; Petty, M. C. "Nanoscale patterning of gold nanoparticles using an atomic force microscope." *Mater. Sci. Eng., C.* **2005**, *25*, 33-38.

movement of the tip over the sample surface, either by moving the tip over a stationary surface or through the use of a piezoelectric scanner that moves the sample underneath a stationary tip.[13] The probe tip is attached to a cantilever that responds to changes in height, conductivity, and friction as it is moved across the sample surface. Changes in cantilever deflection are monitored by a laser that is reflected of the front end of the cantilever into a split photodiode detector.[13] The general scheme of a tapping-mode AFM, the instrument used in this research, is shown in Figure 19, but the underlying structure is the same no matter which mode of contact is used**.**

The amount of contact between the probe and the sample is variable. Probe-sample contact ranges from no contact at all (non-contact mode) to constant contact (contact mode). In tapping mode, an intermediate between constant contact and none, the tip regularly "taps" or touches the surface of the sample as it scans.[13] In non-contact and tapping modes, the cantilever oscillates at or slightly above its resonance frequency. Non-contact mode is generally considered to be the most finicky to set up and produces the lowest resolution images of the three methods, but also has the least damaging effect on the sample because the tip never touches the sample surface. At the other extreme, atomic-scale resolution can be achieved when using contact mode, but care must be taken to keep the force (controlled by a feedback loop and the instrument's setpoint) low enough to prevent damage to the sample.[13] An important application of contact mode, dip-pen nanolithography depends on the ability of the probe tip to pick up atoms (e.g., gold) and re-deposit them on another area of the sample.[12]

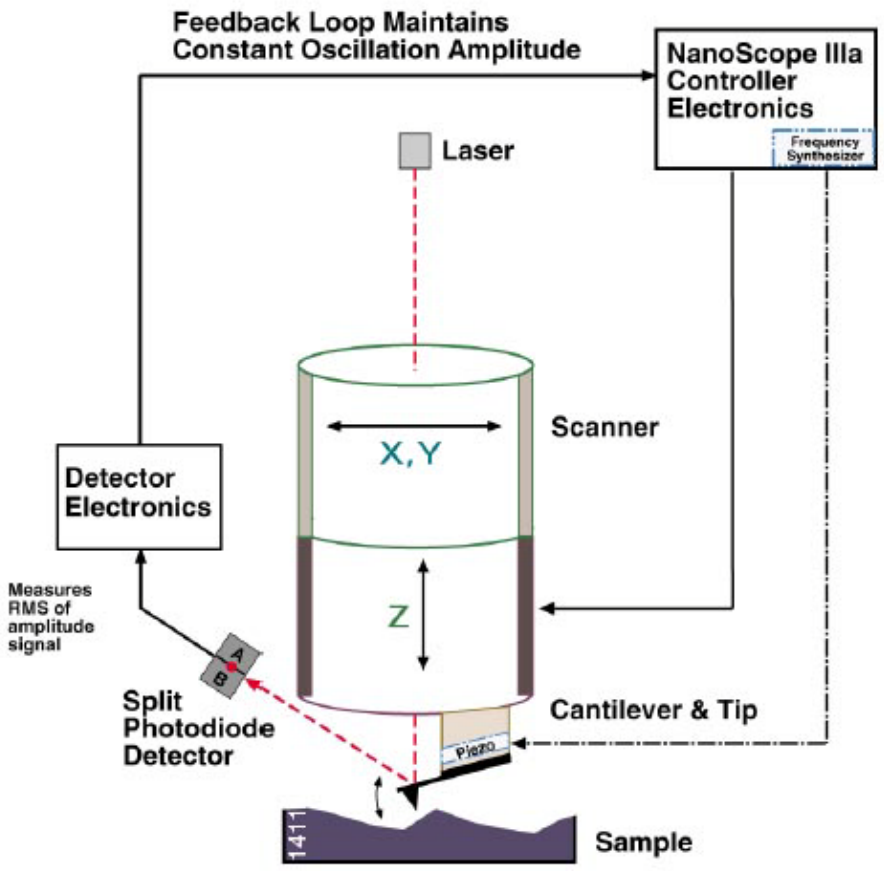

Figure 19: Schematic of a tapping-mode atomic force microscope.[12]

As the probe tip is moved across the sample, electrostatic forces cause its height to change as a function of the height, friction constant, or rigidity of the sample. In tapping mode, the AFM employs a feedback loop so that it can keep the root-mean-square (RMS) of the oscillation signal at a constant value. This feedback loop is also used to maintain constant force on the sample in contact mode and constant cantilever oscillation in non-contact mode. Images can be generated from the measurement of cantilever deflection to show height, deflection, or a number of other methods of measurement.[12]

One limit of AFM resolution is tip size. Tapping mode tips typically have a radius of curvature of 5-10 nm.[13] The probe tip must be smaller than the features being imaged in order to obtain a clear/accurate picture of surface morphology. A tip that is damaged or too wide will not accurately track the sample surface. This problem particularly affects lateral resolution, so that a feature's actual dimensions do not directly correspond with those imaged by the AFM. Although lateral resolution is better for tapping mode than for contact mode, the lateral dimensions indicated by the probe are still often exaggerated, representing objects as larger than they actually are. Many scientists prefer to use height information in determining the shape of their samples rather than measuring lateral dimensions.[10,13] In image formation, micrographs with sides on the length of micrometers can be produced. For a specific Veeco instrument (Dimension 3100), maximum image size in the x- and y-directions is about 100 μm, while the tip can track objects in the z-direction up to 6 μm in height.[12]

Preparation of Materials

Single layer Langmuir-Schaefer films were made by depositing tri-*n*-octylphosphine oxide-capped Ag nanoparticles in 12, 30, and 80 nm sizes onto freshly-cleaved muscovite mica sheets. The nanoparticles were manufactured by Meliorum Technologies, Inc. (Rochester, NY) and were washed 10x with chloroform prior to use by suspending in 1 mL chloroform, microfuging, and discarding the supernatant. Photon correlation spectroscopy data provided from the manufacturer gives actual sizes of 12.4±3.7 nm, 34.2±7.1 nm, and 74.2±8.8

nm (mean ± standard deviation). The mica was purchased from Electron Microscopy Sciences, Hatfield, PA. Films were made using the horizontal dip method on a NimaPro Nima516 LB (Langmuir-Blodgett) Trough, manufactured by Nima Technology Ltd. The trough was cleaned three times with chloroform before each sample was prepared. The trough was filled with Millipore MilliQ deionized water (resistivity 18.2 MΩ cm^{-1}) and any visible dust was aspirated from the surface of the water subphase.

The particles were suspended in chloroform at variable concentrations of 0.38-1.8 mg/mL and sonicated for 35 minutes. The three samples described later, which formed the only consistent monolayers, were all prepared from the same suspension of particles with a concentration of 1.22 mg/mL. Prior to each deposition, a microsyringe was cleaned 10x with chloroform and 5x with the suspension of interest. For each deposition, volumes (150-600 μL) of the chloroform suspension sufficient to reach each target pressure were then deposited dropwise onto the surface of the water layer. Effort was taken to minimize the disruption to the surface tension by allowing a single drop to hang off the end of the microsyringe, which was then gently touched to the water surface to transfer the solution from syringe to trough. The sample was deposited onto the water surface in a systematic grid pattern to minimize the instances where new particles might be dropped on top of previously deposited ones. The trough was left to sit for 15 minutes to allow the solvent to evaporate and the particles to distribute evenly across the surface of the water. Before barrier compression, a freshly-cleaved, 1x2 cm sheet of mica was suspended horizontally

above the trough and lowered to within 2 mm of the water surface. The barriers were set to compress at a speed of 10 cm^2/min until the water surface reached the target pressure. After the target pressure had been reached, the sample holder was gently pressed downward until the mica touched the water surface. The sample was then raised using the trough's "creep up" function at a rate of 1 mm/min until it reached its maximum height, where it was left to dry for a few minutes before it was removed to a covered container. Both the purchased nanoparticles and the finished films were stored in a desiccator.

Samples were prepared for all particle sizes across a range of low, medium, and high surface pressures, where low pressure has been defined as < ~7 mN/m, medium pressure designates the range ~8-12 mN/m, and high pressure represents pressures > 15 mN/m. The initial target pressures were 5, 12, and 20 mN/m, although the final samples characterized for the 12 nm particles were deposited at surface pressures of 7.1, 11.9, 15.8, and 17.8 mN/m. The samples prepared with 30 and 80 nm particles were found to have almost nonexistent nanoparticle monolayers, a result which is discussed below.

Characterization

Unless otherwise noted, the films were imaged using a Veeco/Digital Instruments Dimension 3100 AFM in tapping mode equipped with Veeco phosphorous (n) doped silicon tips (fc: 293-387 kHz, k: 20-80 N/m). Micrographs were taken of each sample in 5x5 and 10x10 μm sizes with a resolution of 512 lines/image. Height and phase channels were recorded. A Veeco diInnova AFM

equipped with Veeco phosphorous (n) doped silicon tips (fc: 237-309 kHz, k: 20-80 N/m) was also used in tapping mode.

The films were also analyzed via Fourier transform infrared spectroscopy (FTIR) using a MIDAC Corporation M Series FTIR Spectrophotometer. A background scan of a blank mica sample (cleaved and adhered to and removed from the LB dipping mechanism) of 200 repeats at 4 cm^{-1} was taken prior to the spectra of the samples. Spectra of the films were taken for 200 repeats at a resolution of 4 cm^{-1} for several locations on each sample. When a low signal-to-noise ratio persisted, spectra were also taken with 300 scans.

Results and Discussion

Langmuir-Schaefer monolayers were prepared with 12 nm TOPO-capped silver nanoparticles. The monolayers were deposited at trough surface pressures of 7.1, 11.9, 15.8, and 17.8 mN/m. A series of tapping mode AFM micrographs were taken for each film. Figures 20 and 21 show 10x10 and 5x5 μm height images for each sample.

Pre-deposition particle clumping has remained a persistent problem but has been reduced through the proper sonication of the particles in suspension (use of a vial with greater surface area, such as a 20 mL scintillation vial, is recommended over a 1-2 mL volumetric flask). Clumps seen in the AFM of the 12 nm particles were less than 27nm high, the height of 2 particles, suggesting that they formed in situ on the trough surface as the barriers compressed and were not a product of pre-deposition clumping. It is expected that clumps formed

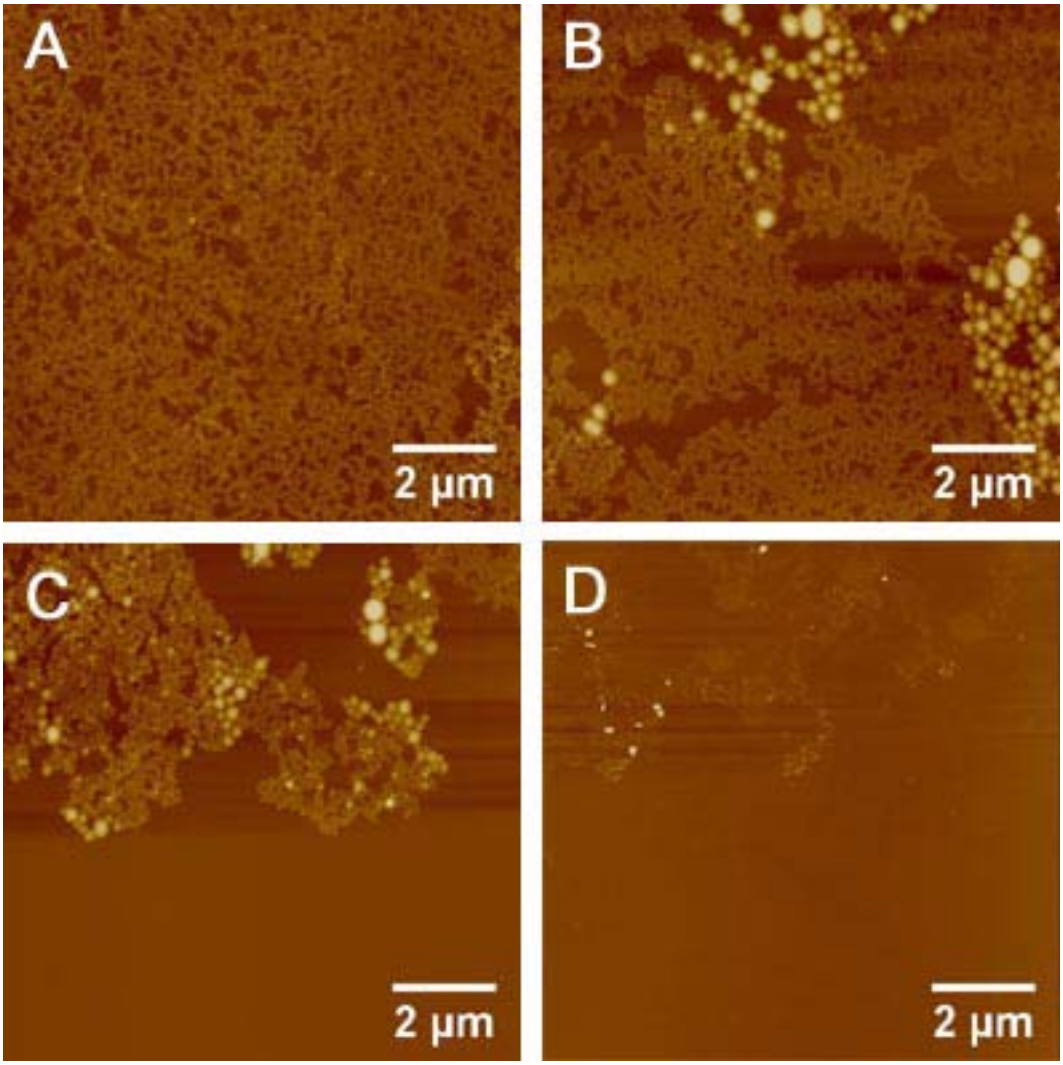

Figure 20: AFM (height images) of 12 nm TOPO-capped silver nanoparticle Langmuir-Schaefer monolayers at deposition pressures of (a) 7.1 mN/m, (b) 11.9 mN/m, (c) 15.8 mN/m, and (d) 17.8 mN/m. Images are 10 x 10 μm.

before particle dispersal and compression would be larger and more irregularly shaped. This can be seen in the monolayer cross-sections shown in Figures 22 and 23.

At all surface pressures, the particles are closely networked with each other. At the lowest pressure, 7.1 mN/m (Figures 20a, 21a, and 22a), the sample shows extensive coverage, with many evenly-distributed small domains, disrupted

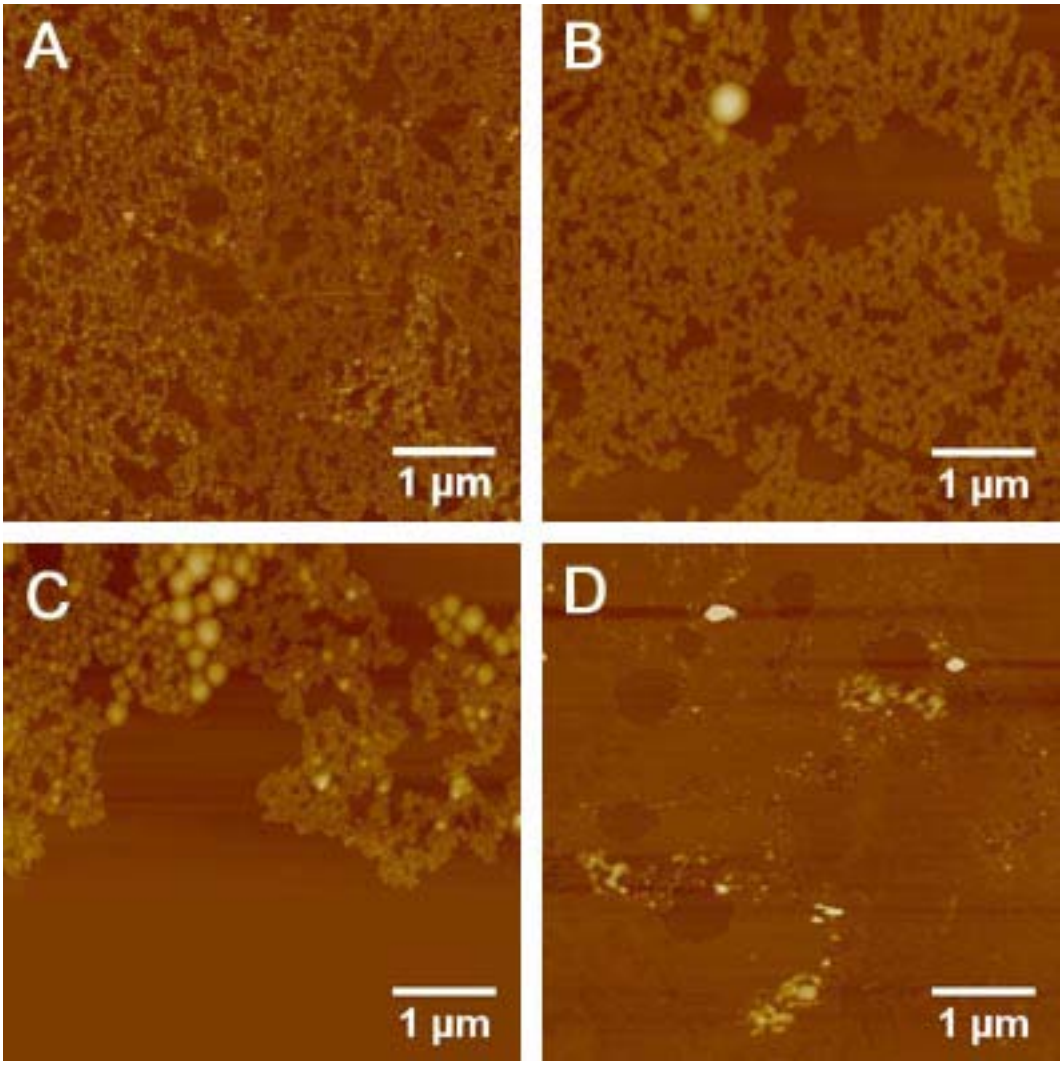

Figure 21: AFM (height images) of 12 nm TOPO-capped silver nanoparticle Langmuir-Schaefer monolayers at deposition pressures of (a) 7.1 mN/m, (b) 11.9 mN/m, (c) 15.8 mN/m, and (d) 17.8 mN/m. Images are 5 x 5 µm.

by small, evenly distributed defects. However, this sample has some areas very similar in appearance to the nanoparticle monolayer that can be shown from cross-section information to be smaller (~2.5-5 nm) than the accepted range of particle sizes. These differences are not immediately visible in the AFM without using a narrowly defined height scale or performing cross-sectional analysis. Even on the size range of 10x10 µm, the low pressure monolayer has even particle

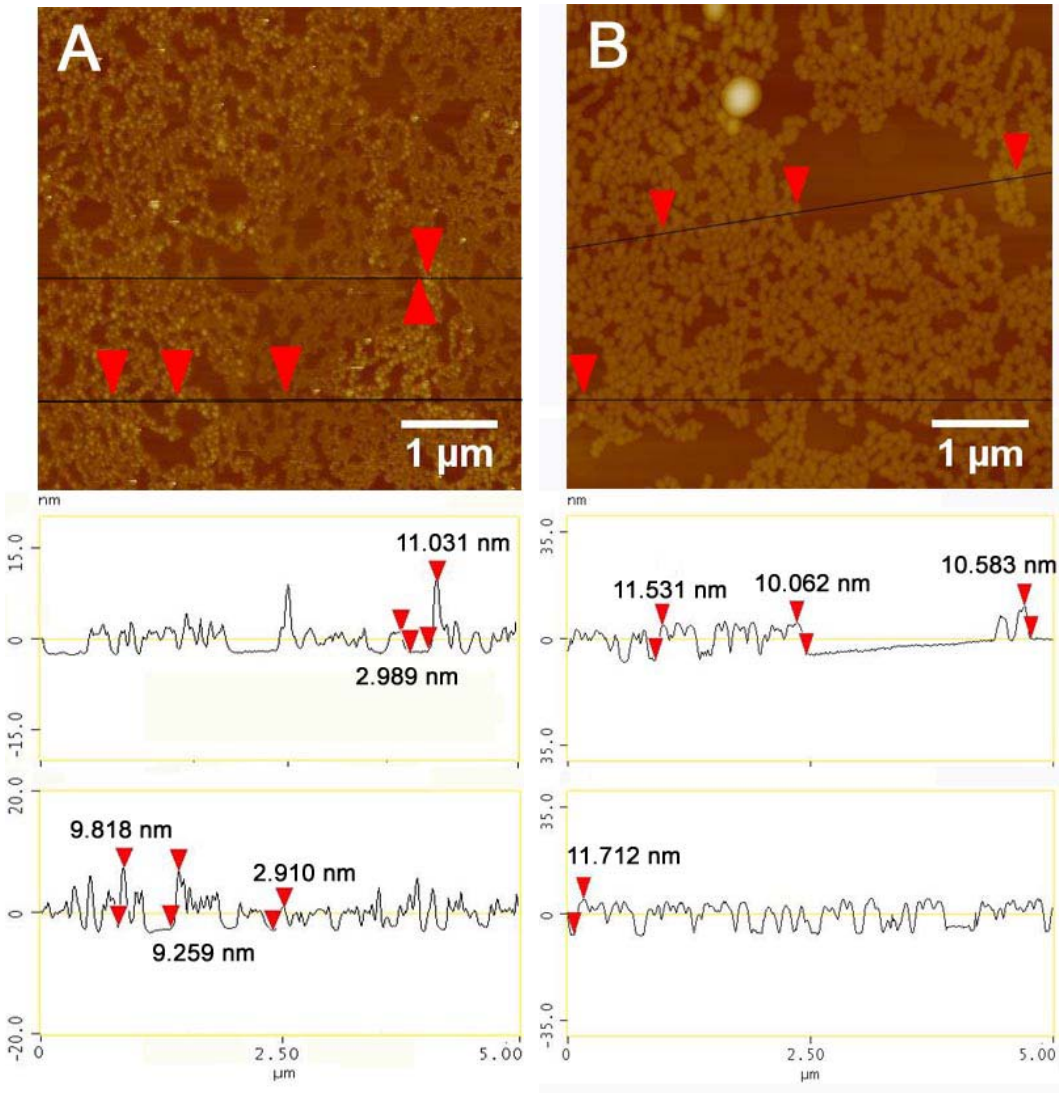

Figure 22: AFM (height images) of 12 nm TOPO-capped silver nanoparticle Langmuir-Schaefer monolayers at (a) 7.1 mN/m and (b) 11.9 mN/m. Two height profiles are displayed for each sample. Both show consistent presence of 12 nm particles, although (a) also indicates some clumps, the height of two stacked particles, and sections of the lower-profile TOPO monolayers. The distance between the pointers is indicated.

density and fairly close packing, with few clumps. Assuming a spherical silver particle with a diameter of 12 nm, the calculated area per particle for this sample was 2218 nm^2. (The cross-sectional area of a 12 nm sphere is 452.4 nm^2.)

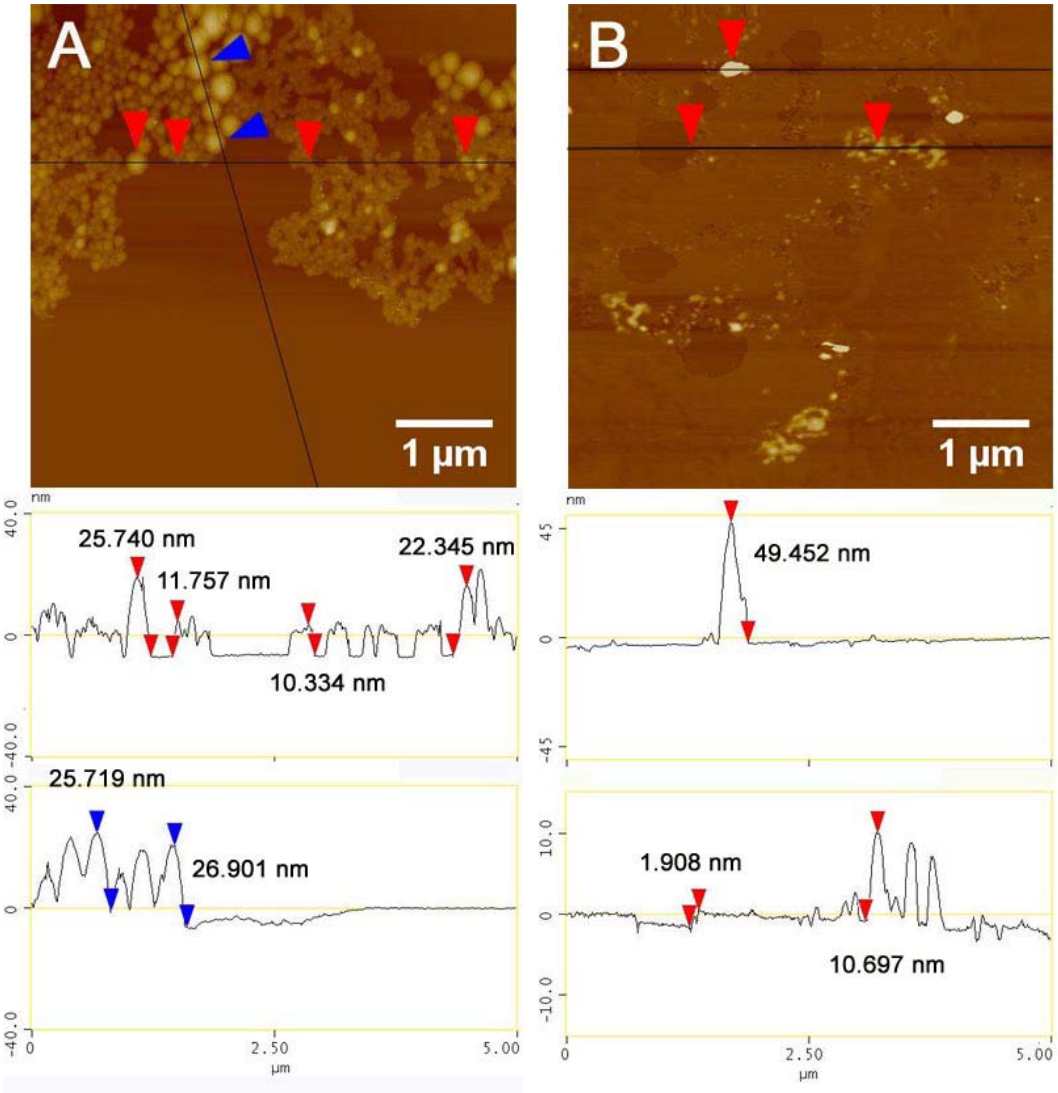

Figure 23: AFM (height images) of 12 nm TOPO-capped silver nanoparticle Langmuir-Schaefer monolayers at (a) 15.8 mN/m and (b) 17.8 mN/m. Two height profiles are displayed for each sample. (a) has height profiles consistent with the deposition of 12 nm particles, while (b) has areas of very low height (TOPO monolayer) and larger particle clumps in addition to 12 nm particles. The distance between the pointers is indicated.

In the medium pressure monolayer, 11.9 mN/m (Figures 20b, 21b, and 22b), the particles have arranged into large, more closely packed domains, with an average area/particle of 1504 nm^2. Considerably larger monolayer defects are also

present. Within the large domains, the particles are better-packed than those of the low pressure sample, but small, pervasive defects are still common in this film.

The high pressure sample, 15.8 mN/m (Figures 20c, 21c, and 23a), has the largest, most densely packed particle domains, but it also has the largest defects and a large number of particle clumps. Average area/particle for this sample was 1107 nm^2. Height profiles of the high-pressure film show that the clumps range in height from about 22 to 27 nm, the height of two nanoparticles stacked together. It is hypothesized that under the highest pressure, the particles have been compressed to the point of aggregation and that the large clumps interfere with monolayer formation. Compression was done at the slowest possible trough speed (10 cm^2/min), but the samples were not given a resting period in which to equilibrate between barrier compression and mica deposition. Although unlikely to solve or reverse the problem of particle clumping under higher pressures, a rest period may help the low to medium pressure samples to become even more regularly distributed.

The 17.8 mN/m sample (Figures 20d, 21d, and 23b) did not form an acceptable monolayer but is presented as an example of the interference of loose TOPO molecules in monolayer formation. As seen in Fig. 23b, this sample has a number of ovoid (~0.75 μm diameter) defects in the monolayer where the blank mica surface is exposed. From the height profiles, it can be seen that this monolayer coverage is not, for the most part, nanoparticles. Rather, the height at the edges of the monolayer is ~2 nm, as would be expected for a pure TOPO monolayer. There are a few 10-12 nm features, indicating the presence of

nanoparticles, as well as two larger features, but the sample displays both poor nanoparticle coverage and poor TOPO coverage. The same preparation technique was used for cleaning the nanoparticles in all cases, but the 17.8 mN/m sample was manufactured 4.5 months after the other three samples described here, approximately 14 months after the capped nanoparticles were synthesized. It seems most likely that the problem in preparing the monolayer comes from poor bonding between the silver particles and their organic capping ligand, causing TOPO to separate from the particles during the sonication process. The manufacturer suggests that the particles may no longer be stable after 6 months.

A number of attempts were made to synthesize layers using a similar procedure for 30 and 80 nm TOPO-capped silver nanoparticles. When examined under an optical microscope, these samples had a large number of visible features—round, dark clumps—which may be dust and debris or may be evidence of particle clumping. These features were too high for AFM imaging, but imaging done on the “clean” areas of the surface showed very few particles present. In many cases, the surface was consistently lightly textured with a few smooth areas of blank mica. Height measurements (<2 nm) were taken at the edges of these regions. The surface texture and low feature height suggests that these samples contain pure or almost-pure TOPO monolayers. The images of the attempted 30 and 80 nm particle monolayers are consistent with those taken of particle-free TOPO surfaces, such as that displayed in Figure 24.

Preliminary research into the preparation of capped silver nanorods monolayers has shown that sonication time has an effect on the size of nanorod

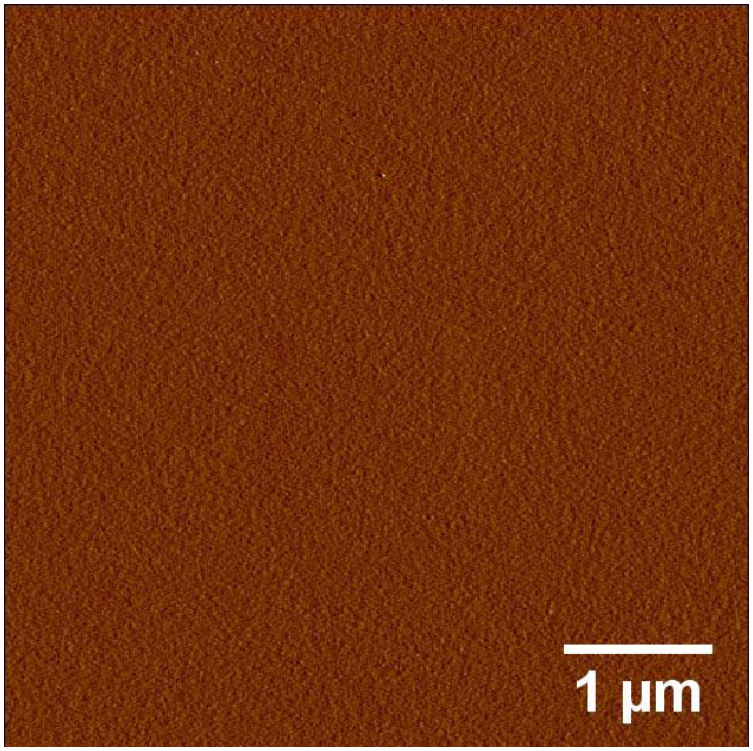

Figure 24: A Langmuir-Blodgett monolayer of loose TOPO at 24.8 mN/m

clumps and, ultimately, rod integrity. If left to sonicate for too long, the rods are broken into pieces smaller than the manufacturer's specified size.[14] It is suggested that prolonged sonication also has a fragmenting effect on the nanoparticles, explaining the lack of appropriately sixed features in AFM images of 30 and 80 nm monolayers. Figure 25 is an AFM image, taken with the Veeco diInnova AFM, of an 80 nm nanoparticle monolayer deposited at 11.8 mN/m. Although this monolayer visually appears to have the same characteristic packing as the 12 nm nanoparticle films, the features measure well above the expected 80 nm height.

TOPO-capped nanoparticles and loose TOPO produce isotherms with different slopes. When comparing the isotherms for the 12 nm samples detailed

[14] Song, J; Jayathilake, H. D. Mount Holyoke College, South Hadley, MA. Unpublished results.

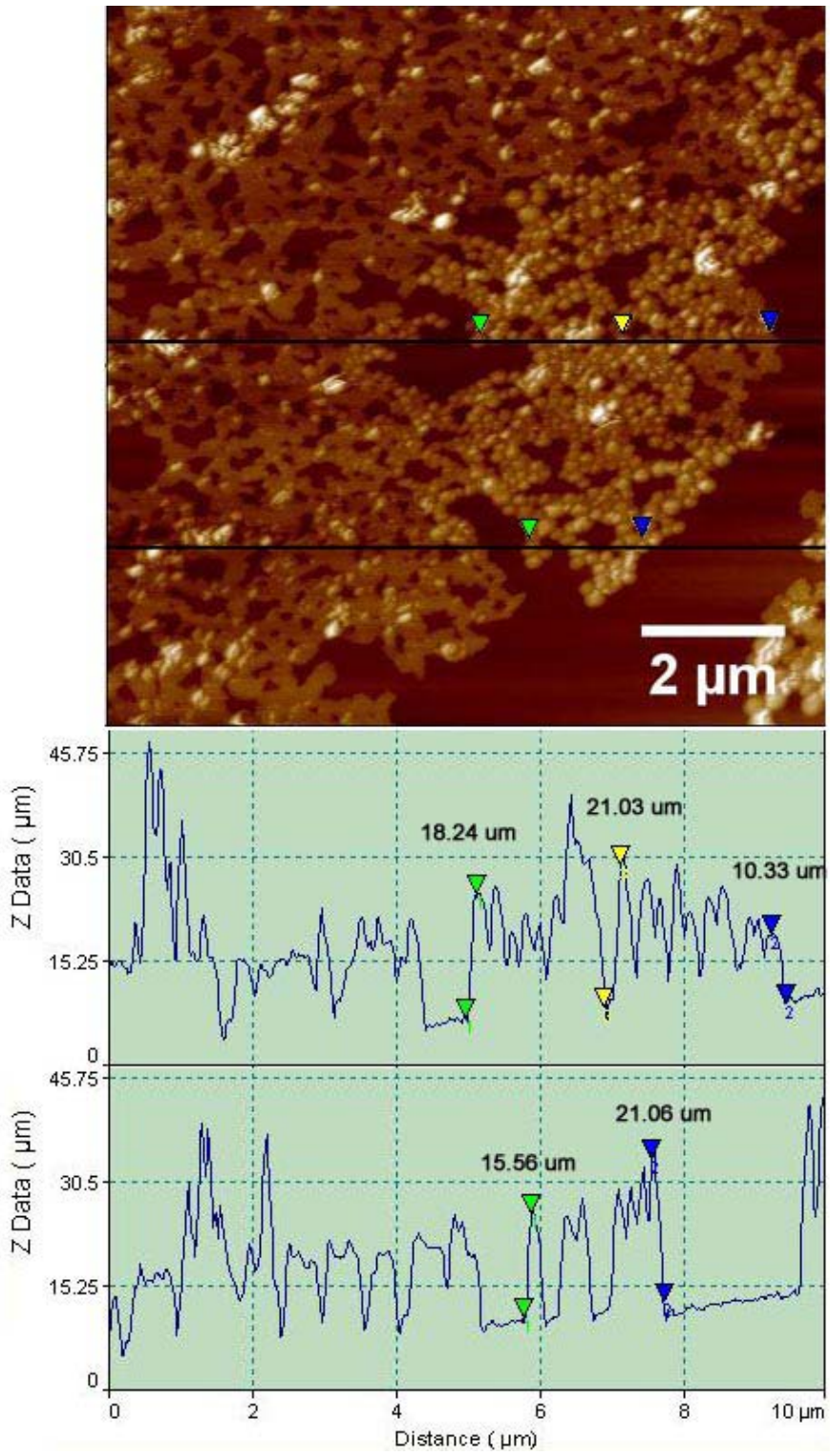

Figure 25: An AFM image of a 80 nm TOPO-capped silver nanoparticle Langmuir-Schaefer monolayer deposited at 11.8 mN/m. All of the features are too large to be 80 nm particles. This image was taken with a Veeco diInnova AFM in tapping mode.

above, Figure 26, it can be seen that they have similar shapes and parallel slopes (the point at which the surface pressure begins to increase significantly above zero depends on the amount and concentration of the substance dispersed on the water surface, which was different for each of the monolayer preparations shown here). A comparison of the nanoparticle isotherms with that of loose TOPO molecules (Figure 26) shows that the TOPO-only isotherm has a sharper slope as it moves into the liquid expanded phase. The isotherms for the seemingly-blank samples were checked against a standard TOPO isotherm and were found to have the same sharper slope, matching the isotherm for loose TOPO molecules and not matching the isotherm for capped nanoparticles. This suggests that very few nanoparticles were present on the water surface during the compression process. The amount of loose TOPO present may be due to prolonged sonication cleaving TOPO from the surface of the nanoparticles.

The lack of features of significant height, similarity in texture to TOPO-only surfaces, and evidence from the deposition isotherms support a hypothesis that the larger nanoparticles did not properly deposit onto the surface. The features that are visible under the light microscope may be normal debris and contamination or may be indicative of the particles forming large clusters rather than remaining a distinct monolayer. X-ray photoelectron spectroscopy or other trace elemental analysis may be helpful in determining if the visible clumps contain any silver nanoparticles or nanoparticle fragments. The sonication step is helpful in breaking up these aggregates but it can be seen with the naked eye that the particles form new clumps within minutes of sonication and settle to the

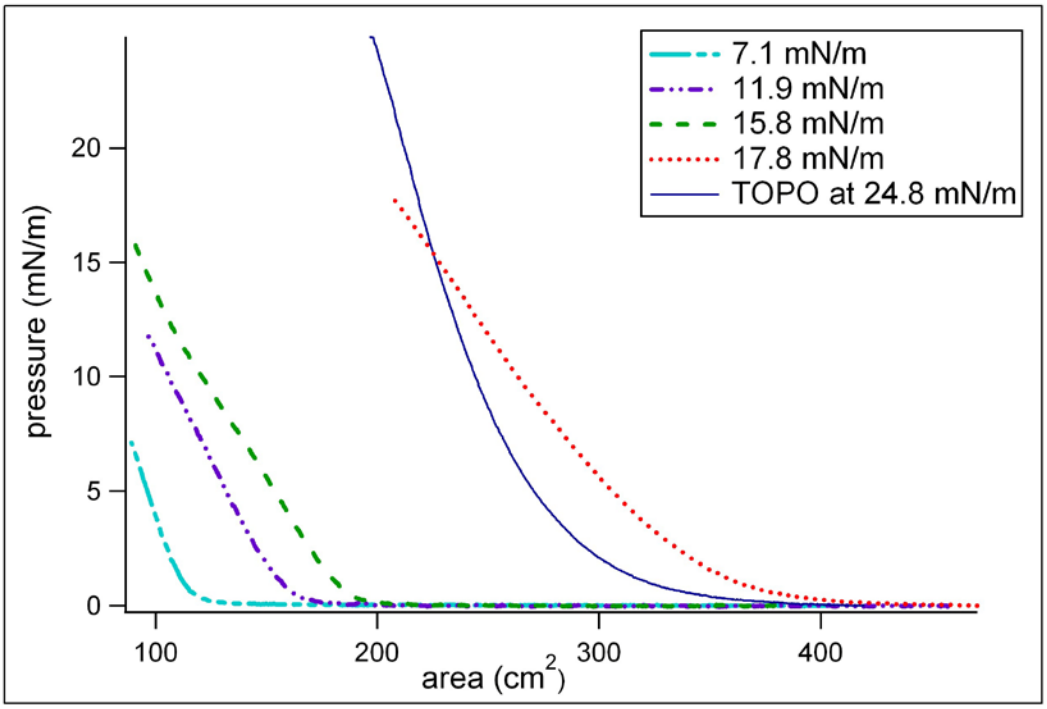

Figure 26: Isotherms from the preparation of 12 nm TOPO-capped silver nanoparticle Langmuir-Schaefer monolayers at a variety of surface pressures (dashed lines). A comparison with a pure TOPO monolayer (solid line) shows that the two systems have distinctively different isotherms.

bottom of the vial. This process happens more rapidly for larger, heavier particles. One possible explanation for the lack of success in forming these monolayers is that the particles are clumping and forming large aggregates on the water surface that either sink or do not stick to the mica during deposition. The isotherms indicate that there is something present on the water surface when compression begins, but their slope suggests that that substance is largely TOPO and contains few nanoparticles. Three possible explanations exist: the nanoparticles are clumping and sinking before compression; aggregation decreases the number of distinct entities on the water surface such that they have a reduced effect on the interaction of the mostly-TOPO monolayer; or they are sinking to the bottom of

the flask so quickly after sonication that not many are initially drawn into the syringe.

Fourier transform infrared spectroscopy (FTIR) confirmed the presence of TOPO in 12 and 80 nm nanoparticle monolayers. These spectra are displayed in Figure 27. The peak at 1420-1440 cm^{-1} is indicative of CH_3 and CH_2 bending vibration. The mica substrate provided too much interference for resolving other significant bands in the spectra. When TOPO was deposited directly onto a NaCl plate, bands were visible for CH_3/CH_2 vibration, CH stretching (2840-3000 cm^{-1}), and $R_3P=O$ stretching (1150-1190 cm^{-1}). These bands are all expected for an alkylphosphine oxide and are displayed in Figure 28.[15]

Scanning electron microscopy (SEM) was used to image samples made from 12, 30, and 80 nm particles and deposited on silicon wafers. Similar packing trends were observed, however, individual particles could not be resolved to confirm these results.[16] More particles are present, forming larger islands, when the deposition surface pressure is higher.

The networked patterning of nanoparticles on mica substrates, as imaged by AFM, is paralleled by similar patterning of the same particles on silicon wafers, imaged by SEM. Further investigation of particles on silicon by AFM would provide a good point of comparison. The mica-based samples cannot be imaged via SEM because the high energy electron beam would damage the mica surface. Transmission electron microscopy (TEM) would also make a nice addition to the characterization techniques for this project because of the TEM's ability to define

[15] Pretsch, E; Bühlmann, P; Badertscher, M. *Structure Determination of Organic Compounds: Tables of Spectral Data*, 4th ed.; Springer-Verlag: Berlin, 2009.
[16] Jayathilake, H. D; Rice, M. Mount Holyoke College, South Hadley, MA. Unpublished results.

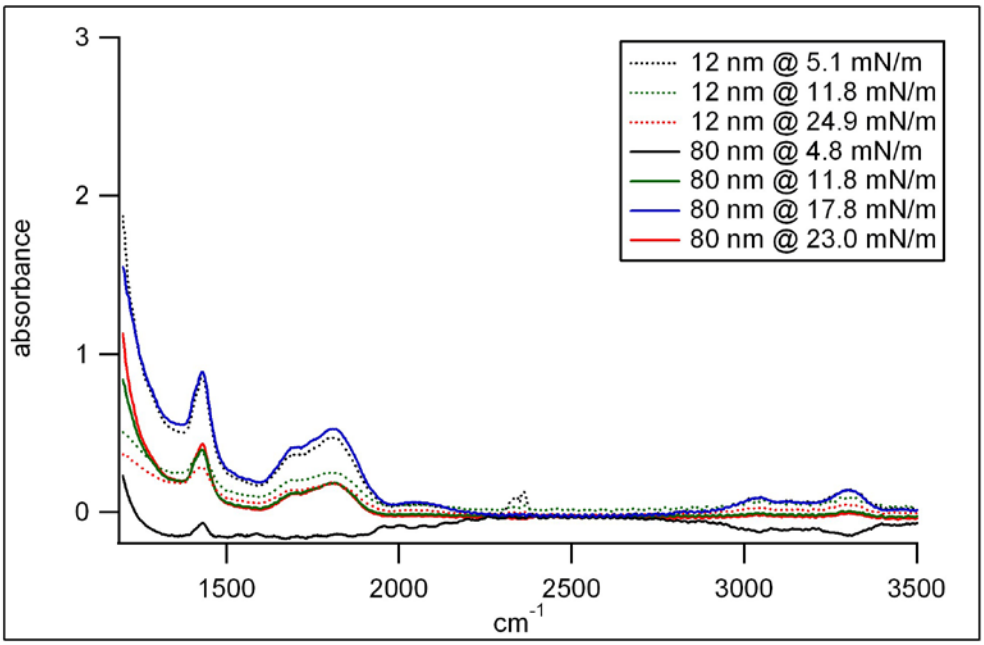

Figure 27. FTIR spectra of 12 and 80 nm TOPO-capped silver particle films compressed to surface pressures of (12 nm films) 5.1, 11.8, and 24.9 mN/m and (80 nm films) 4.8, 11.8, 17.8, and 23.0 mN/m. There was too much interference from the mica substrate, even with background removal, to depict clear bands in the sub-1400 cm^{-1} range, where the P=O stretching band is expected. The broad band at ~3400 cm^{-1} comes from moisture in the air.

edges and horizontal distances more precisely than an AFM. The preparation of LS films on TEM grids is currently being investigated. Substrate hydrophobicity is an important factor to consider in the preparation of all of these additional films. Because hydrocarbon-capped nanoparticles are hydrophobic, they should exhibit greater affinity for mica substrates, which are less hydrophilic than silicon substrates. Carbon-coated TEM grids should support even stronger bonding between the particles and the substrate.

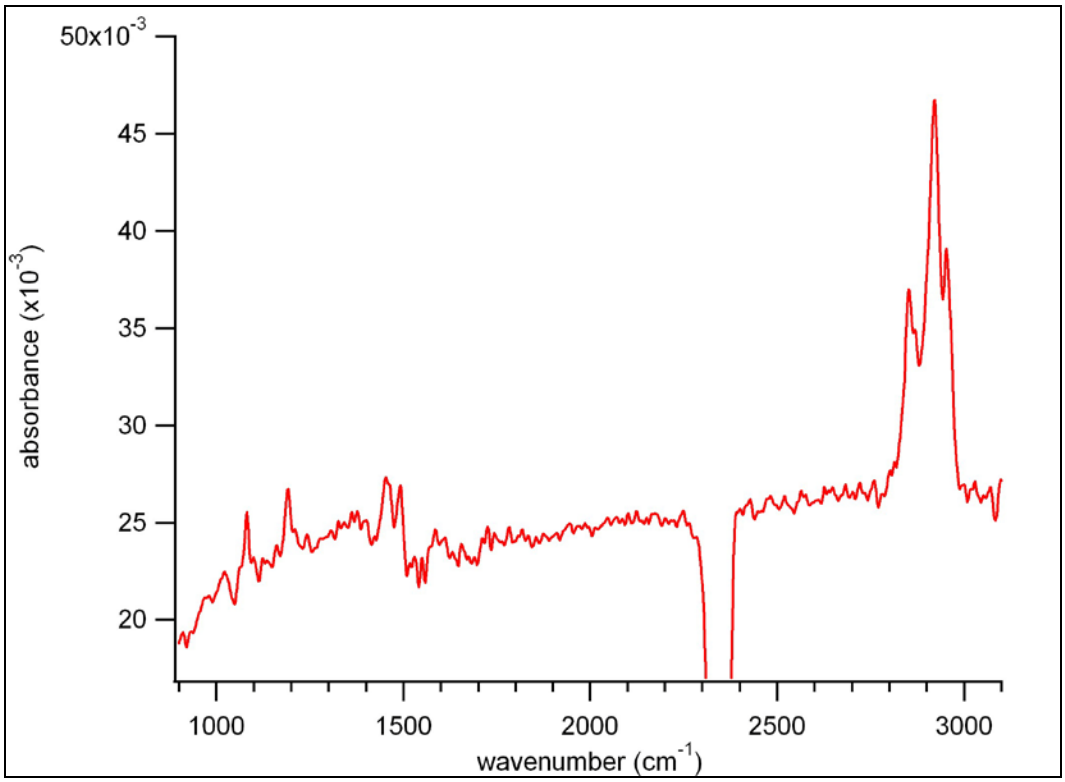

Figure 28: FTIR of TOPO on a NaCl plate. Without interference from mica, the bands for CH_2/CH_3 bending vibration (1420-1440 cm^{-1}), CH stretching (2840-3000 cm^{-1}), and P=O stretching (1150-1190 cm^{-1}) are visible.

Conclusion

12 nm TOPO-capped silver nanoparticles were used in the manufacture of Langmuir-Schaefer monolayers on muscovite mica substrates. The monolayers were deposited at surface pressures of 7.1, 11.9, 15.8, and 17.8 mN/m. The low pressure sample exhibited good monolayer coverage and even particle distribution and had fewer defects and aggregates. The particle packing was as expected. The medium (11.9 mN/m) and high (15.8 mN/m) samples had comparably larger monolayer defects due to particle aggregation. The highest pressure, 17.8 mN/m, did not see successful nanoparticle monolayer formation, but is included to show

examples of more extreme nanoparticle clumping and the formation of TOPO-only monolayers in lieu of a nanoparticle film.

Future work includes an investigation into the optimum sonication period for the different sizes of nanoparticles at different concentrations. The choice of a more hydrophobic substrate will improve the successful transfer of the nanoparticle film from the water surface to the substrate. It is possible that adding a resting period after barrier compression and before monolayer deposition will allow the layer to better equilibrate and even-out the monolayer density.

Conclusion

Nanoparticles' small sizes give them many unique optical and electronic properties. The experience quantum confinement effects that cause many of these properties, such as the vibrant colors of metal nanoparticles, to be size-dependent.[1,2,3] They have applications in catalysis, magnetic recording, and ceramics,[1] as well as uses as colorants for stained glass[2] and as antimicrobial agents.[4]

The small sizes that make nanoparticles so interesting also present unique challenges for characterization. Transmission electron microscopy and atomic force microscopy have been explored as two methods that image materials at nano-scale resolutions. Nanoparticle assembly has also been explored through the use of Langmuir-Blodgett and Langmuir-Schaefer monolayer deposition.

The first part of this project quantified the rate of phase transformation from ferrihydrite to goethite, two different iron oxide species, when ferrihydrite suspensions are treated with phosphate, Fe(II), and alizarin. It also qualitatively examined the transformation of a sugar-treated ferrihydrite sample into goethite, curved goethite rods, and hematite.

---

[1] Wang, Z. L, Ed. *Characterization of Nanophase Materials*. Wiley-VCH: New York, 2000.
[2] Kelly, K. L; Coronado, E; Zhao, L. L; Schatz, G. C. "The Optical Properties of Metal Nanoparticles: The Influence of Size, Shape, and Dielectric Environment." *J. Phys. Chem. B* **2003**, *107*, 668-677.
[3] Zhang, Q; Tan, Y. N; Xie, J; Lee, J. Y; "Colloidal Synthesis of Plasmonic Metal Nanoparticles." *Plasmonics* **2009**, *4*, 9-22.
4 Rai, M; Yadav, A; Gade, A. "Silver nanoparticles as a new generation of antimicrobials." *Biotechnol. Adv.* **2009**, 27, 76-83.

The second part of this project investigated the optimum deposition pressure for the formation of Langmuir-Schaefer monolayers of TOPO-capped silver nanoparticles. It was found that increasing the surface pressure increases the number of nanoparticle clumps and defects in the monolayer and that the monolayers deposited at lower pressures, in the range of 7 to 12 mN/m, had more even nanoparticle coverage.

Literature Cited

Introduction

1. Wang, Z. L, Ed. *Characterization of Nanophase Materials*. Wiley-VCH: New York, 2000.
2. "Sharper Image Introduces FresherLonger™ Miracle Food Storage Containers." Business Wire. March 8, 2006. Accessed April 20, 2010. <http://www.nsti.org/press/PRshow.html?id=867>
3. Rai, M; Yadav, A; Gade, A. "Silver nanoparticles as a new generation of antimicrobials." *Biotechnol. Adv.* **2009**, 27, 76-83.
4. Cai, W; Gao, T; Hong, H; Sun, J. "Applications of gold nanoparticles in cancer nanotechnology." *Nanotechnol., Sci. Appl.* **2008,** *1*, 17–32.
5. Skumryev, V; Stoyanov, S; Zhang, Y; Hadjipanayis, G; Givord, D; Nogués, J. "Beating the superparamagnetic limit with exchange bias." *Nature* **2003**, *423I*, 850-853.
6. Song, X; Huang, L; Wu, B. "Bright and Monodispersed Phosphorescent Particles and Their Applications for Biological Assays." *Anal. Chem.* **2008**, *80*, 5501-5507.
7. Kelly, K. L; Coronado, E; Zhao, L. L; Schatz, G. C. "The Optical Properties of Metal Nanoparticles: The Influence of Size, Shape, and Dielectric Environment." *J. Phys. Chem. B* **2003**, *107*, 668-677.
8. Zhang, Q; Tan, Y. N; Xie, J; Lee, J. Y; "Colloidal Synthesis of Plasmonic Metal Nanoparticles." *Plasmonics* **2009**, *4*, 9-22.
9. "Zetasizer Nano Series User Manual." MAN0317, Issue 2.1. Malvern Instruments Ltd. Worcestershire, United Kingdom. July 2004.
10. Cornell, R. M; Schwertmann, U. *The iron oxides: structure, properties, reactions, occurrences and uses*. Wiley VCH: New York, 2003.
11. Schwertmann, U; Cornell, R. M. *Iron Oxides in the Laboratory: Preparation and Characterization*. VCH Publishers, Inc.: New York, 1991.
12. Penn, R. L; Erbs, J. J; Gulliver, D. M. Controlled growth of alpha-FeOOH nanorods by exploiting-oriented aggregation. *J. Cryst. Growth* **2006**, *293*, 1-4.
13. Moskowitz, B. M. "Hitchhiker's Guide to Magnetism." Institute for Rock Magnetism, University of Minnesota, 1991. Accessed March 2010. <http://www.irm.umn.edu/hg2m/hg2m_index.html>

Chapter 1

1. Cornell, R. M; Schwertmann, U. The iron oxides: structure, properties, reactions, occurrences and uses. Wiley VCH: New York, 2003.

2. Erbs, J. J; Gilbert, B; Penn, R. L. Influence of Size on Reductive Dissolution of Six-Line Ferrihydrite. *J. Phys. Chem. C* **2008**, *112*, 12127-12133.
3. Schwertmann, U; Cornell, R. M. *Iron Oxides in the Laboratory: Preparation and Characterization*. VCH Publishers, Inc.: New York, 1991.
4. Michel, F. M; Ehm, L; Antao, S. M; Lee, P. L; Chupas, P. J; Liu, G; Strongin, D. R; Schoonen, M. A. A; Phillips, B. L; Parise, J. B. The Structure of Ferrihydrite, a Nanocrystalline Material. *Science* **2007**, *316*, 1726-1729.
5. Penn, R. L; Tanaka, K; Erbs, J. Size dependent kinetics of oriented aggregation. *J. Cryst. Growth* **2007**, *309*, 97-102.
6. Kung, K.-H; McBride, M. B. Electron transfer processes between hydroquinone and iron oxides. *Clays Clay Miner.* **1988**, *36*, 303.
7. Penn, R. L; Erbs, J. J; Gulliver, D. M. Controlled growth of alpha-FeOOH nanorods by exploiting-oriented aggregation. *J. Cryst. Growth* **2006**, *293*, 1-4.
8. Moskowitz, B. M. "Hitchhiker's Guide to Magnetism." Institute for Rock Magnetism, University of Minnesota, 1991. Accessed March 2010. <http://www.irm.umn.edu/hg2m/hg2m_index.html>
9. Burleson, D. J; Penn, R. L. Two-Step Growth of Goethite from Ferrihydrite. *Langmuir* **2006**, *22*, 402-409.
10. Yuwono, V. M; Burrows, N. D; Soltis, J. A; Penn, R. L. Oriented Aggregation: Formation and Transformation of Mesocrystal Intermediates Revealed. *J. Am. Chem. Soc.* **2010**, *132*, 2163–2165.
11. Penn, R. L. Kinetics of Oriented Aggregation. *J. Phys. Chem. B* **2004**, *108*, 12707-12712.
12. Niederberger, M; Cölfen, H. Oriented attachment and mesocrystals: Non-classical crystallization mechanisms based on nanoparticle assembly. *Phys. Chem. Chem. Phys.* **2006**, *8*, 3271-3287.
13. Penn, R. L. "Transmission Electron Microscopy." Accessed December 2008. <http://www.chem.umn.edu/groups/penn/tem.html>
14. Flegler, S. L; Heckman, J. W. Jr; Klomparens, K. L. *Scanning and Transmission Electron Microscopy: An Introduction*. Oxford University Press: New York. 1993.
15. Williams, D. B; Carter, C. B. *Transmission Electron Microscopy: A textbook for materials science*. Plenum Press: New York, 1996.
16. FEI Company. "Magellan XHR Scanning Electron Microscope." <http://www.fei.com/products/scanning-electron-microscopes/magellan.aspx> Accessed February 2010.
17. National Center for Electron Microscopy. "Microscopes and Facilities: OÅM." <http://ncem.lbl.gov/frames/oam.htm> Accessed April 2010.
18. Yuwono, V. M; Burrows, N. D; Soltis, J. A; Penn, R. L. Oriented Aggregation: Formation and Transformation of Mesocrystal Intermediates Revealed. *J. Am. Chem. Soc.* **2010**, *132*, 2163–2165.
19. "A Review of the Universe" <http://universe-review.ca/I11-41-tem.jpg> Accessed December 2008.
20. Burrows, N. D; Yuwono; V; Penn, R. L. "Quantifying the Kinetics of Crystal Growth by Oriented Aggregation." *Mater. Res. Bull.* **2010**, *35*, 133-137.

21. Müller, S.A.; Aebi, U.; Engel, A. “What transmission electron microscopes can visualize now and in the future.” *J. Struct. Biol.* **163** (2008) 235-245.
22. Jentzsch, T. L; Penn, R. L. Influence of Aluminum Doping on Ferrihydrite Nanoparticle Reactivity. *J. Phys. Chem. B* **2006,** *110*, 11746-11750.

Chapter 2

1. Lambert, K; Čapek, R. K; Bodnarchuk, M. I.; Kovalenko, M. V; Van Thourhout, D; Heiss, W; Hens, Z. “Langmuir-Schaefer Deposition of Quantum Dot Multilayers.” *Langmuir*. **Article ASAP**. Web publication February 3, 2010.
2. Ji, X; Wang, C; Xu, J; Zheng, J; Gattá-Asfura, K. M; Leblanc, R. M. “Surface Chemistry Studies of (CdSe)ZnS Quantum Dots at the Air-Water Interface.” *Langmuir* **2005**, *21*, 5377-5382.
3. Tatewaki, Y; Noda, Y; Akutagawa, T; Tunashima, R; Nori, S; Nakamura, T; Hasegawa, H; Mashiko, S; Becher, J. “Langmuir-Blodgett Films Constructed from a Charge-Transfer Complex and Gold Nanoparticles.” *J. Phys. Chem. C* **2007**, *111*, 8871-18877.
4. Tao, A. R; Huang, J; and Yang, P. “Langmuir-Blodgettry of Nanocrystals and Nanowires.” *Acc. Chem. Res.* **2008**, *41*, 1662-1673.
5. Saponjic, Z. V; Csencsits, R; Rajh, T; Dimitrijevic, N. M. “Self-Assembly of TOPO-Derivatized Silver nanoparticles into Multilayered Film.” *Chem. Mater.* **2003**, *15*, 4521-4526.
6. Wang, Z. L, Ed. *Characterization of Nanophase Materials*. Wiley-VCH: New York, 2000.
7. Talham, Daniel R.. “Conducting and Magnetic Langmuir-Blodgett Films.” *Chem. Rev.* **2004**, *104*, 5488.
8. Hąc-Wydro, K.; Wydro, P.; Dynarowicz-Łątka, P. “A study of the interaction between dialkyldimethylammonium bromides and tri-*n*-octylphosphine oxide (topo) in mixed monolayers at the air/water interface.” *Journal of Colloid and Interface Science*. **2004.** *278*, 206.
9. Petty, Michael C. *Langmuir-Blodgett films: An introduction*. Cambridge: Cambridge University Press, 1996. 53-54.
10. Merrett, K; Corneilius, R. M; McClung, W. G; Unsworth, L. D; Sheardown, H. “Surface analysis methods for characterizing polymeric biomaterials.” *J. Biomater. Sci. Polymer Edn.* **2002**, *13*, 593-621.
11. Cross, S. E; Jin, Y-S; Rao, J; Gimzewski, J. K. “Applicability of AFM in cancer detection.” *Nat. Nanotechnol.* **2009**, *4*, 72-73.
12. “Scanning Probe Microscopy Training Notebook.” Version 3.0. Digital Instruments, Veeco Metrology Group, 2000.
13. Prime, D; Paul, S; Pearson, C; Green, M; Petty, M. C. “Nanoscale patterning of gold nanoparticles using an atomic force microscope.” *Mater. Sci. Eng., C.* **2005**, *25*, 33-38.
14. Song, J; Jayathilake, H. D. Mount Holyoke College, South Hadley, MA. Unpublished results.
15. Pretsch, E; Bühlmann, P; Badertscher, M. *Structure Determination of Organic Compounds: Tables of Spectral Data*, 4th ed.; Springer-Verlag: Berlin, 2009.

16. Jayathilake, H. D; Rice, M. Mount Holyoke College, South Hadley, MA. Unpublished results.

Conclusion

1. Wang, Z. L, Ed. *Characterization of Nanophase Materials*. Wiley-VCH: New York, 2000.
2. Kelly, K. L; Coronado, E; Zhao, L. L; Schatz, G. C. "The Optical Properties of Metal Nanoparticles: The Influence of Size, Shape, and Dielectric Environment." *J. Phys. Chem. B* **2003**, *107*, 668-677.
3. Zhang, Q; Tan, Y. N; Xie, J; Lee, J. Y; "Colloidal Synthesis of Plasmonic Metal Nanoparticles." *Plasmonics* **2009**, *4*, 9-22.
4. Rai, M; Yadav, A; Gade, A. "Silver nanoparticles as a new generation of antimicrobials." *Biotechnol. Adv.* **2009**, 27, 76-83.